UNIVERSIDADE DE SÃO PAULO
INSTITUTO DE FÍSICA DE SÃO CARLOS

José Yitzhak Aarón Chacaliaza Ricaldi

Thin films based on Er^{3+} doped germanate-tellurite nanoglasses for Plasmonics

São Carlos

2023

José Yitzhak Aarón Chacaliaza Ricaldi

Thin films based on Er^{3+} doped germanate-tellurite nanoglasses for Plasmonics

Dissertation presented to the Graduate Program in Physics at the Instituto de Física de São Carlos da Universidade de São Paulo, to obtain the degree of Master in Science.

Concentration area: Theoretical and Experimental Physics

Advisor: Prof. Dr. Euclydes Marega Junior

Corrected version
(Original version available on the Program Unit)

São Carlos
2023

Ricaldi, José Yitzhak Aarón Chacaliaza
Thin films based on Er3+ doped germanate-tellurite nanoglasses for Plasmonics / José Yitzhak Aarón Chacaliaza Ricaldi; advisor Euclydes Marega Junior - corrected version -- São Carlos 2023.
97 p.

Dissertation (Master's degree - Graduate Program in Theoretical and Experimental Physics) -- Instituto de Física de São Carlos, Universidade de São Paulo - Brasil , 2023.

1. Glasses. 2. Thin films. 3. Rare-earths ions. 4. Ligth-matter interaction. 5. Plasmonics. I. Marega Junior, Euclydes, advisor. II. Title.

Este trabajo está dedicado a mis padres y abuelos.

ACKNOWLEDGEMENTS

First of all, I would like to thank God for life and for everything He has blessed me with during this time. I would also like to express my gratitude to my parents, José and Lucy, for their love towards me and the support they have given me throughout this journey.

I would like to thank my advisor during this master's period, Prof. Dr. Euclydes Marega Jr., for his trust and unconditional support. Thank you for welcoming me into your laboratory at the University of São Paulo (USP) and providing all the facilities to carry out this master's dissertation. I would also like to extend my heartfelt thanks to Prof. Dr. Victor Anthony Garcia Rivera from the Centre d'Optique, Photonique et Laser (COPL), Canada, who played a fundamental role in the development of this research. Thank you for your guidance and patience on this scientific path that started in Peru and continued in Brazil. I hope to continue working together for a long time. Similarly, I want to thank Dr. José Luis Clabel Huaman and Mg. Gaston Lozano Calderon for their support when I arrived in São Carlos, for the discussions on solid-state physics, optics, and photonics. Truly, your contributions have been very important for the development of this dissertation.

Special thanks to all those who supported this master's dissertation, especially to Mg. Iago Carvalho Pinto and Prof. Dr. Younès Messaddeq from the COPL, for their collaboration in the fabrication of the glass samples. Thanks to Prof. Dr. Rogeria Rocha Gonçalves from the Faculty of Philosophy, Sciences, and Letters of Riberão Preto–USP, for the support in refractive index and lifetime measurements, to Prof. Dr. Ariano De Giovanni Rodrigues from the Department of Physics–UFSCar, for the support in Raman spectroscopy and UV-Vis-NIR absorption measurements, and to Prof. Dr. Danilo Manzani from the Institute of Chemistry of São Carlos–USP, for the support in XRD and FTIR measurements.

Special thanks to those who made homesickness (*saudades*) more bearable during these years in Brazil and made me feel at home. Thank you to Republica Gato Preto for welcoming me when I arrived in São Carlos, and for all the moments shared and beers enjoyed during this time. Also, thanks to the Peruvian community in São Carlos for the barbecues (*churrascos*) and moments of togetherness.

This study was financed in part by the Coordenação de Aperfeiçoamento de Pessoal de Nível Superior (CAPES) – Brasil – Finance Code 001, Process 88887.643238/2021-00, and also with the support of the Fundação de Amparo à Pesquisa do Estado de São Paulo through the Center for Research in Optics and Photonics, Process 2013/07276-1.

"Amat victoria curam"
Virgílio

ABSTRACT

RICALDI, J. Y. A. C. **Thin films based on Er^{3+} doped germanate-tellurite nanoglasses for Plasmonics**. 2023. 97p. Dissertation (Master in Science) - Instituto de Física de São Carlos, Universidade de São Paulo, São Carlos, 2023.

Er^{3+}-doped germanate-tellurite glasses were synthesized using the conventional melt-quenching technique. The glass samples were melted at 900 °C and subsequently subjected to heat treatment at 290 °C. Optical characterization of the glasses included refractive index measurements, photoluminescence, radiative lifetime decay, and UV-VIS-NIR absorption spectroscopy were performed. Additionally, the influence of Er^{3+} doping on the glass structure was investigated using FTIR, Raman spectroscopy, and X-ray diffraction. The second part of this dissertation focused on fabricating nanostructured glasses (nanoglasses) and plasmonic metasurfaces on gold thin film. The nanoglasses were mixed in a solution of polymethyl methacrylate and deposited on the metasurfaces using spin-coating. The roughness and thickness of the thin films were characterized using atomic force microscopy and contact profilometry. The luminescence properties of the thin film were examined using fluorescence confocal microscopy. The confocal optical microscopy and confocal lifetime fluorescence techniques were used to investigate the coupling mechanisms between surface plasmons polaritons located on the metasurface and the rare-earth ions. It was observed that when Er^{3+} ions are located close to the surface, there is a strong coupling mechanism between them due to the reduction in the radiative lifetime of the Er^{3+} emitter. This coupling is more evident in smaller nanoparticles, that is, closer to the interface. The results show the possibility of developing photonic devices using this platform.

Keywords: Glasses. Thin films. Rare-earth ions. Light-matter interaction. Plasmonics.

RESUMO

RICALDI, J. Y. A. C. **Filmes finos baseados em nanovidros germânio-telurito dopados con Er^{3+} para Plasmônica**. 2023. 97p. Dissertação (Mestrado em Ciências) - Instituto de Física de São Carlos, Universidade de São Paulo, São Carlos, 2023.

Vidros de germanato-telurito dopados com Er^{3+} foram sintetizados utilizando a técnica convencional de fusão e resfriamento rápido. As amostras de vidro foram fundidas a 900 °C e, posteriormente, submetidas a tratamento térmico a 290 °C. A caracterização óptica dos vidros incluiu medidas de índice de refração, fotoluminescência, decaimento do tempo de vida radiativo e espectroscopia de absorção UV-VIS-NIR. Além disso, a influência do dopamento de Er^{3+} na estrutura do vidro foi investigada utilizando FTIR, espectroscopia Raman e difração de raios X. A segunda parte desta dissertação concentrou-se na fabricação de vidros nanoestruturados (nanovidros) e metassuperfícies plasmônicas em filmes finos de ouro. Os nanovidros foram misturados em uma solução de polimetil-metacrilato e depositados nas metassuperfícies por meio de spin-coating. A rugosidade e a espessura dos filmes finos foram caracterizadas utilizando microscopia de força atômica e profilometria de contato. As propriedades de luminescência do filme fino foram examinadas utilizando microscopia confocal de fluorescência. As técnicas de microscopia óptica confocal e fluorescência com tempo de vida confocal foram usadas para investigar os mecanismos de acoplamento entre polaritons de plasmônio de superfície localizados na metassuperfície e os íons de terras raras. Observou-se que quando os íons Er^{3+} estão localizados próximos à superfície, há um forte mecanismo de acoplamento entre eles devido à redução do tempo de vida radiativo do emissor Er^{3+}. Esse acoplamento é mais evidente em nanopartículas menores, ou seja, mais próximas da interface. Os resultados mostram a possibilidade de desenvolver dispositivos fotônicos usando essa plataforma.

Palavras-chave: Vidros. Filmes finos. Ions de terras raras. Interação luz-matéria. Plasmônica.

LIST OF FIGURES

LIST OF TABLES

LIST OF ABBREVIATIONS AND ACRONYMS

AFM	Atomic force microscopy
BO	bridging oxygen
Er^{3+}	tri-ionized erbium
Er_2O_3	Erbium (III)
ESA	excited state absorption
ET	energy transfer processes
FIB	Focused ion beam
FLIM	Fluorescence lifetime images
FTIR	Fourier Transformed Infrared spectroscopy
FWHM	full width at half maximum
Ga^+	Gallium ions
GeO_2	Germanium dioxide
LPE	Lone-pair electron
LSPR	Localized surface plasmon resonance
NaO_2	Sodium dioxide
NBO	non-bridging oxygen
NIR	Near-Infrared region
nm	nanometers
O_2	oxygen gas
OH^-	hydroxyl ions
PMMA	Polymethyl-methacrylate
RE	Rare-earth
SEM	Scanning electron microscopy
Si	pure Silicon

SiO_2	Silicum dioxide
SPP	Surface plasmon polariton
SPW	Surface plasma wave
$^{2S+1}L_J$	Russell-Saunders notation
TE	transverse electric polarization
TM	transverse magnetic polarization
TeO_2	Tellurium dioxide
TeO_3	Trigonal pyramidal unit
TeO_{3+1}	Distorted trigonal bipyramidal unit
TeO_4	Trigonal bipyramidal unit
Uc	Up-conversion
UV	Ultraviolet region
V	Crystal field potential
Vis	Visible region
Xe	Xenon
XRD	X-ray difraction
ZnO	Zinc oxide

LIST OF SYMBOLS

α	Absorption coefficent
$B(k,q)$	Crystal field parameter
$C_{k,q}$	Racah tensor operator
c	ligth velocity
E_{ph}	phonon energy
cm^{-1}	wavenumber
δ	Excess oxygen
eV	electron-volts
h	Plank's constant
λ	wavelength
m	sample mass
$\mu\mathrm{s}$	microseconds
n	IR photons involved in up-conversion process
n_1	Linear refractive index
n_2	Nonlinear refractive index
$n\mathrm{s}$	nanoseconds
ν	frequency
ω	frequency
$p\mathrm{s}$	picoseconds
R_a	average surface roughness
R_q	square surface roughness
ρ	density
$\rho(R)$	Crystal field charge density
T_g	Glass transition temperature

T_m	Melting temperature
ε_d	dielectic medium permittivity
ε_m	metal medium permittivity
$Y_{k,q}$	spherical harmonic
ζ	Coupling function spin-orbit
$+3$	trivalent

CONTENTS

1 INTRODUCTION

A plasmon is a collective electron excitation in a metallic/dielectric interface.[1] It is a quantized density wave of electrons that can be excited by electromagnetic radiation. When an interface is illuminated by light, its electrons are excited to collectively oscillate at a frequency determined by the properties of the metal and the wavelength of the incident light.[2]

Light-matter interactions play a crucial role in numerous scientific and technological domains. In recent decades, there has been a growing interest in leveraging plasmons to augment these interactions, as plasmons exhibit the remarkable ability to substantially amplify the local electromagnetic field, thus significantly enhancing the intensity of light-matter interactions.[2] Nevertheless, the efficacy of these interactions is frequently impeded by the limited absorption and scattering cross-sections exhibited by many materials. The advent of plasmonic nanostructures has provided a means to overcome these limitations by engendering highly localized and intense electromagnetic fields at nanoscale volumes. These fields can effectively bolster the interaction between light and matter, thus engendering novel applications in sensing, energy harvesting, and optical communication.

Er^{3+}-doped glasses are widely employed as gain media in optical communication systems due to their emission at 1540 nm, a critical wavelength in telecommunications.[3] However, the efficiency of Er^{3+} emission is frequently hampered by the feeble light-host material interaction.[4] Consequently, the integration of plasmonic nanostructures has emerged as a promising approach to enhance the light-matter interaction and increase the emission efficiency of diverse materials.[5,6]

One strategy for enhancing Er^{3+} emission involves depositing a thin layer of gold with nanostructures on the glass. Gold is chosen for its high electrical conductivity, excellent stability, and low oxidation rate. The gold coating facilitates the generation of surface plasmon polaritons, which are collective localized excitations of electrons in the metal that lead to highly concentrated electromagnetic fields. When the Er^{3+}-doped glass is near the gold surface, plasmons are generated, allowing strong coupling with the Er^{3+} transitions and consequent enhancement of their emission. This enhancement arose from the increased local electromagnetic field around the nanostructure, resulting in a higher radiative decay rate and reduced nonradiative losses. More research is needed to optimize the design of these structures and understand the underlying physical mechanisms for the enhancement. The successful application of this approach could lead to the development of more efficient optical communication systems based on Er^{3+}-doped glasses.

This dissertation aims to investigate the enhancement of Er^{3+} emissions and coupling mechanisms through the polariton of surface plasmons in a thin film with diluted glasses nanoparticles in PMMA, with a particular focus on elucidating the plasmon-Er^{3+} coupling mechanisms. The results of this work contribute to the development of new technologies that harness the power of plasmons for enhanced light-matter interactions.

1.1 Objectives

General objectives

Investigate plasmon-Er^{3+} coupling in thin films based on nanostructured germanate-tellurite glass deposited on gold nanostructures.

Specific objectives

- Synthesis of germanate-tellurite glasses doped with Er^{3+} ions at different concentrations and studied the structural and optical properties.
- Synthesize thin films by spin coating based on ground glasses embedded in polymethylmethacrylate on Au nanostructures and study the structural and optical properties.
- Propose a plasmon-Er^{3+} coupling mechanism to explain the luminescence enhancement in the system studied.

1.2 Chapters overview

Chapter 2: The basic theoretical concepts are exposed to give context to the dissertation. First, the definitions of glass in the literature are reviewed. Next, the physics behind the properties of rare earth ions is presented. Finally, the plasmons are contextualized, and their quantization, the formation of surface plasmons polariton, and their main technological applications are explained.

Chapter 3: The synthesis methodology of glasses and thin films is explained. Characterization techniques used to study the optical and structural properties of the samples were presented.

Chapter 4: The influence of Er^{3+} doping on the glasses' structural, optical, and luminescent properties are presented and discussed.

Chapter 5: Then the experimental results of the nanoparticle photoluminescence thin films are presented, and the mechanism of plasmon-Er^{3+} coupling is discussed.

Chapter 6: Finally, in this chapter, the results' conclusions are argued, and future perspectives related to this research are mentioned.

2 STATE OF ART

A current problem in nanophotonics is the coupling between surface plasmons polaritons (SPP) and quantum emitters (such as rare earth ions), which depends on their distance. A proposed solution for the coupling problem is to reduce the dimensions of the system to the nanometer scale to guarantee a strong coupling.[6,7] In this dissertation, the use of thin films obtained from glasses doped with rare earth ions deposited on gold nanostructures is proposed, for which it was considered relevant to review the state of the art of glasses (with emphasis on tellurite glasses), rare-earth ions (with emphasis on Er^{3+} ions) and Plasmonics, which is presented below.

2.1 Glasses

Glasses have played an essential role in the advancement of modern civilization. Morse and Evenson, 2016[8] argue that we currently reside in the Age of Glass, while the United Nations General Assembly declared 2022 the International Year of Glass. However, there remains an ongoing debate within the scientific community regarding the precise definition of glass. The American Society for Testing and Materials defined glass in 1945 as an inorganic molten substance that has solidified without crystallizing.[9] Nevertheless, the discovery of organic, polymeric, and metallic alloy glasses in the last century challenges this definition. Furthermore, natural glasses like obsidian and amber have existed long before the emergence of life on Earth[10], and it is even conceivable that a significant portion of the water in the Universe exists in a glassy state.[11]

Table 1 – Modern definitions of glass.

Author	The glass definition is:
E. Mari, 1982[12]	an amorphous solid obtained by rapidly cooling a molten mass, preventing its crystallization.
J. Zarzycki, 1982[13]	a non-crystalline solid that exhibits the glass transition phenomenon.
J. Shelby,1997[14]	an amorphous solid with complete lack of order and long-range periodicity, displaying a glass transition region.
K. J. Rao, 2002[15]	a solid obtained by supercooling a liquid that is amorphous to X-rays.
A. K. Varshneya, 2010[16]	a solid with a non-crystalline structure that continually changes to a liquid on heating.
E. D. Zanotto, 2017[17]	a non-equilibrium, non-crystalline state of condensed matter that exhibits a glass transition. The structure of the glasses is similar to that of their supercooled liquid predecessors.

Source: By the author.

Table 1 shows the modern definitions of glasses in the literature. A concept often repeated in modern definitions of glass is the phenomenon of glass transition, and to define this term, we consider the formation of glass from the melting of materials, so the glass transition is defined as the intersection between a glassy region and a liquid region, as shown in Figure 1, starting from a material at its melting temperature (T_m), and considering that the material is gradually cooled, in a given moment it will reach the glass transition temperature T_g, and under these conditions, it is like a supercooled and extremely viscous liquid. Finally, this material will change phase, reaching the glassy state.[18] In Figure 1, the red line represents the molten material (liquid). A glass or a crystal can be formed depending on whether the cooling rate is fast or slow.[17]

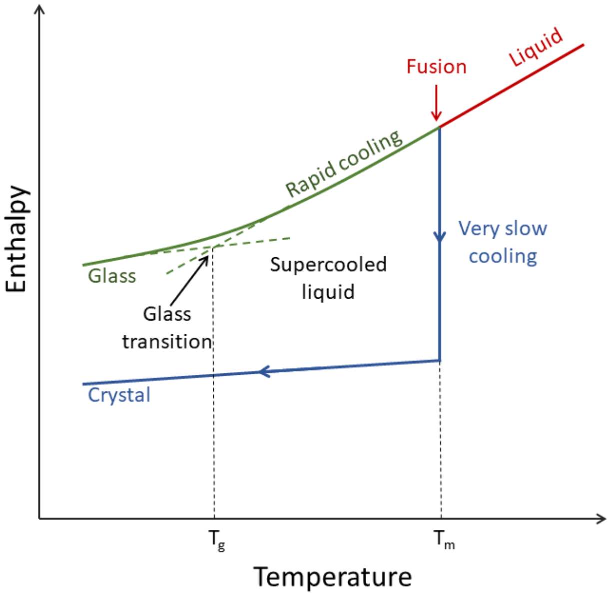

Figure 1 – Graphic representation of glass transition temperature.

Source: Adapted from ZANOTTO *et al.*, 2017.[17]

2.1.1 Tellurium oxide-based glasses

Glasses present interesting properties and technologically relevant applications in health, energy conversion, and photonics.[19–24] In this scenario, Tellurium dioxide (TeO_2) is a conditional glass former, which means that it cannot form a glassy structure by itself (unlike SiO_2 and GeO_2). Still, incorporating a solute (such as ZnO and NaO_2) increases the tendency to form glass considerably.[25,26]

The explanation is that the structure of TeO_2 has a lone pair electron (LPE) in Te^{4+}, which reduces the total number of possible permutations to form a glassy structure. Therefore, the multivalent cations of the so-present with the LPE give rigidity to the vitreous system and reduce the electrostatic repulsion produced by the LPE.[27,28] TeO_2 has three basic structural units (see Figure 2), each containing an LPE: TeO_4, trigonal bipyramid (tbp): Composed of 4 oxygen atoms that are linked by covalent bonds with the central atom of Te and form the tbp; TeO_4, trigonal pyramid (tp): When Te-O bonds are broken, trigonal pyramids are created, where two sites are bridging oxygen (BO) and one nonbridging oxygen (NBO), which is a Te=O double bond and a distorted tbp with TeO_{3+1}: it is the distortion of the tbp due to the presence of excess oxygen (δ).[29,30]

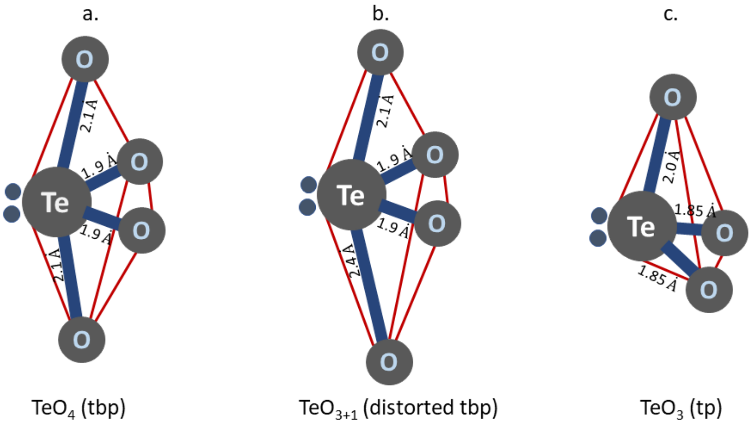

Figure 2 – Schematic representation of structural units in tellurite glass: a. tpb TeO_4, b. distorted tbp TeO_{3+1}, c. tp TeO_3. Dots represent LPE.

Source: Adapted from MANNING *et al.*, 2012.[31]

Tellurite glasses offer a unique combination of a wide transparency range, high rare-earth solubility, low melting temperature, and chemical stability, making them an attractive choice for applications in optics and photonics. Table 2 reports the different optical, thermal, and structural properties of different types of glasses that are important in technological development and are compared with tellurite glasses.

Table 2 – Comparison of the properties of different types of glasses.

Properties	TeO_2	GeO_2	SiO_2	Fluoride	Chalcogenide
Refractive index n_1	1.9 – 2.3	1.7 – 1.8	1.46	1.4 – 1.6	2 – 3.3
Nonlinear refractive index n_2 (m^2W^{-1})	2.5×10^{-19}	10^{-19}	10^{-20}	10^{-21}	10^{-22}
Phonon energy (cm^{-1})	780	880	1100	500 - 630	350
Bandgap (eV)	3.0	3.5 – 4.0	10.0	9.0 – 11.0	1.3 – 3.0
Glass transition temperature T_g $(°C)$	280 – 480	450	1000	270 - 300	140 - 210
Binding type	covalent	covalent	covalent	ionic	covalent
Chemical stability	good	good	high	moderate	moderate
RE solubility	high	good	low	good	low

Source: Adapted from JHA *et al.*, 2012.[32]

2.2 Rare-earth ions

Rare-earth (RE) ions refer to the ions of elements from the RE element series in the periodic table, specifically lanthanides.[33] RE ions are often found in compounds, and the properties of these compounds are influenced by the oxidation state and coordination environment of the RE ions and have a partially filled 4f electron shell, which gives them unique magnetic, optical, and electronic properties, compared to other elements.[34] Due to these properties, RE ions are widely used in various fields, such as electronics, renewable energy, and medical imaging[35]. They play a crucial role in modern technologies, and their high demand has led to increased research and exploration of RE deposits. In glasses, RE ions with valence +3 (trivalent) are found, these being the most stable.

The electronic configuration is $[\mathrm{Xe}]4\mathrm{f}^n$, with 54 electrons and more n electrons in the 4f shell, where $n = 1, 2, \ldots, 14$. Therefore, the electronic configuration of the trivalent RE ions would be as follows: $1\mathrm{s}^2 2\mathrm{s}^2 2\mathrm{p}^6 3s^2 3\mathrm{p}^6 3\mathrm{d}^{10} 4\mathrm{s}^2 4\mathrm{d}^{10} 4\mathrm{f}^n 5\mathrm{s}^2 5\mathrm{p}^6$. The unique properties of RE ions arise from the low radial expansion of their 4f electronic orbitals. These orbitals are screened by the external 5s and 5p electron shells. Their valence electrons are, therefore, less sensitive to their chemical surroundings, while transitions between energy levels into the incomplete 4f electron shell usually result in sharp absorption and emission bands ranging from the UV to the middle infrared (MIR).[34]

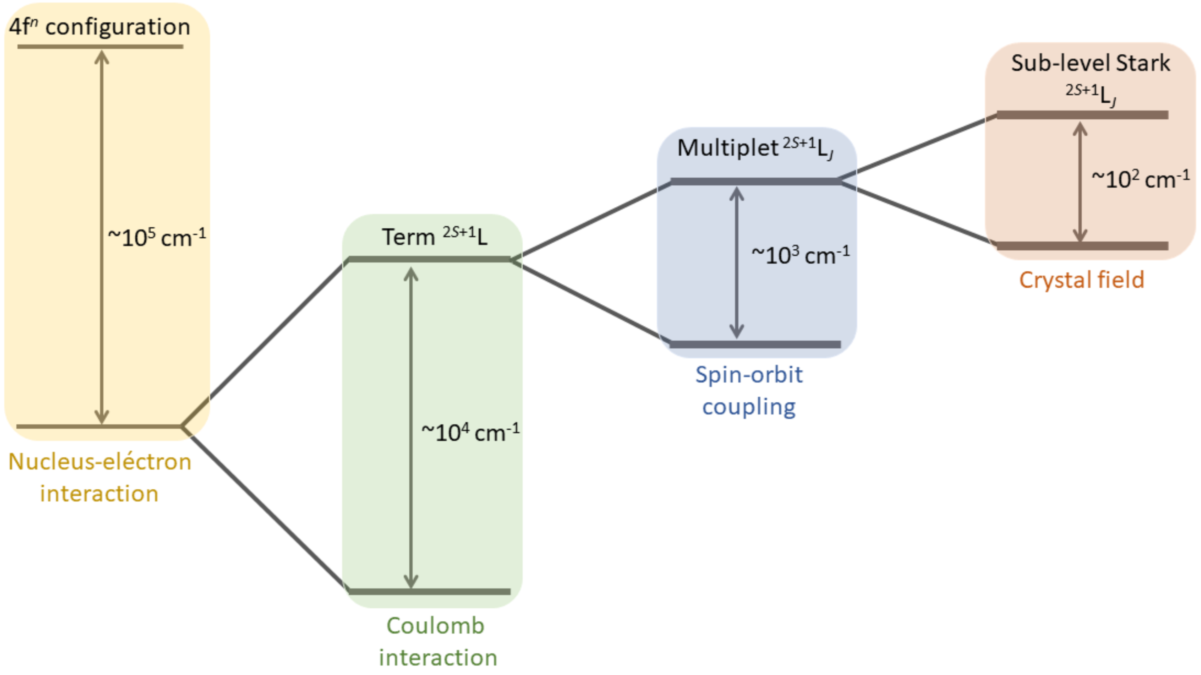

Figure 3 – RE ions Hamiltonian and degeneracy of the energy levels as a function of the type of interaction.

Source: Adapted from RIVERA *et al.*, 2017.[34]

To determine the energy levels of multi-electronic systems such as RE ions, a Hamiltonian is required that considers the interactions of the $4f^n$ electrons with the remaining charge density inside the same ion[34]:

$$H = -\frac{\hbar^2}{2m}\sum_{i=1}^{n}\nabla_i^2 - \sum_{i=1}^{n}\frac{Z^* e^2}{r_i} + \sum_{i<j}^{n}\frac{e^2}{r_{ij}} + \sum_{i=1}^{n}\zeta\left(r_i\right) s_i \cdot l_i + V \tag{2.1}$$

The first term of equation 2.1 defines the kinetic energy of the $4f^n$ electrons; the second term is the potential energy of interaction of the 4felectrons ^{n} with the nucleus. The third term describes the mutual Coulomb interaction between the $4f^n$ electrons, the fourth term represents the spin-orbit interaction, both are responsible for the structure of the energy levels of the $4f^n$ electrons and finally, the fifth term is the contribution of the crystal field which produces a division of the energy levels due to Stark splitting.[34] The spectral position of the energy levels results from the combination of these interactions and the increasing degeneracy of the RE ions' energy levels due to these perturbations. The order of magnitude of the energies involved is represented schematically in Figure 3. The electronic transitions between these levels are described under the following selection rules: $\Delta S = 0;\ \Delta L = \pm 1;\ \Delta J = \pm 1$.

An interesting phenomenon some RE ions exhibit is the up-conversion process (Uc), where RE ions absorb photons of infrared radiation in a matrix material.[36] Then, the electrons in the RE ions are excited to higher energy levels, producing emissions of shorter-wavelength light. In general, near-infrared (NIR) light is converted to ultraviolet (UV), visible (VIS), and anti-Stokes-shifted NIR light (see Figure 4). Light emission can occur in one or more stages, depending on the material and the specific process. Uc processes are used in various applications, including display screen manufacturing, lighting, biotechnology, and medicine. For example, RE Uc materials can produce high-efficiency solar cells, light and temperature sensors, and imaging probes for medical diagnostics.[37,38]

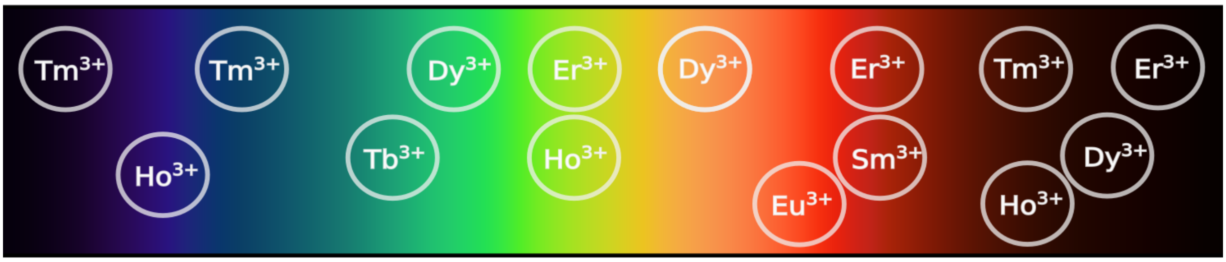

Figure 4 – RE ions exhibit different emission spectral bands under NIR excitation, spanning from NIR to VIS and UV regions.

Source: Adapted from SINGH *et al.*, 2019.[38]

Uc mechanisms are based on the state excited absorption (ESA) between RE ions. Several up-conversion mechanisms exist, such as two-photon up-conversion, three-photon up-conversion, and up-sensitization. Two-photon Uc is a process in which a low-energy (near-infrared) photon is absorbed by a RE ion, which is in a low-energy state. The absorbing photon promotes the ion to a higher-energy state, and then the ion returns to its original state by emitting a high-energy (visible or ultraviolet) photon. This process can be repeated multiple times, resulting in the Uc of low-energy photons to high-energy photons.[39] Three-photon Uc is similar to two-photon Uc, except that three low-energy photons are required to promote the RE ion to a higher energy state before the emission of a high-energy photon. Because a higher density of low-energy photons is required for three-photon Uc, this process is less efficient than two-photon Uc.[39] Up-sensitization is a mechanism in which a "sensitizer" RE ion is used to increase the efficiency of Uc into another "emitter" RE ion. The sensitizing ion absorbs a low-energy photon and transfers the energy to the emitting ion through a process known as Forster resonance energy transfer. This up-sensitization mechanism increases the efficiency of Uc since the emitting ions can absorb low-energy photons that they could not absorb directly.[39]

2.2.1 Erbium

The optical properties of Er^{3+} are determined by its electronic structure, which consists of a partially filled 4f shell with a ground state configuration of $[Xe]4f^{11}6s^2$. This configuration is stable due to the partially filled 4f shell, which gives rise to many energy levels and optical transitions.[34] Furthermore, Er^{3+} is also used in luminescent materials, such as phosphors, to enhance their brightness and efficiency. Er^{3+} can be incorporated into various host materials. Its 4f electrons do not participate in chemical bonding, making it an ideal candidate for fluorescence and luminescence applications. The energy levels of Er^{3+} are represented in the Dieke diagram as shown in Figure 5, which are expressed as ${}^{2S+1}\mathrm{L}_J$ (Russell-Saunders notation), where S is the total spin quantum number of the electrons of the atom. The value $2S+1$ written in the symbol of the term is the spin multiplicity, which is the number of possible values of the magnetic spin quantum number m_S for a given spin S, J is the total angular momentum quantum number for the electrons of the atom, has a value in the range from $|L-S|$ to $L+S$ and L is the total orbital quantum number in spectroscopic notation.

Er^{3+} is a luminescent ion, which means it absorbs light at one wavelength and emits longer wavelengths.[40] This property is useful in optical fiber communication, where Er^{3+} is commonly used as a dopant in optical fiber amplifiers to amplify signals at the 1550 nm wavelength, which is a commonly used wavelength range for optical communication.[41,42] In biomedical applications, Er^{3+} can be used in biocompatible materials for in vivo imaging and therapy due to its efficient fluorescence in the near-infrared region.[43–45] This is important because near-infrared light can penetrate deep into biological tissues, which makes Er^{3+} a useful tool for non-invasive imaging and therapy applications.[46] In addition, Er^{3+}-doped materials are promising for sensing applications due to their absorption and emission spectra being sensitive to temperature, making them well-suited for temperature-sensing applications.[47–49] One such application is nano thermometry, where the temperature of a small volume of material is measured with high precision and accuracy and the ability to perform non-invasive measurements.[50,51]

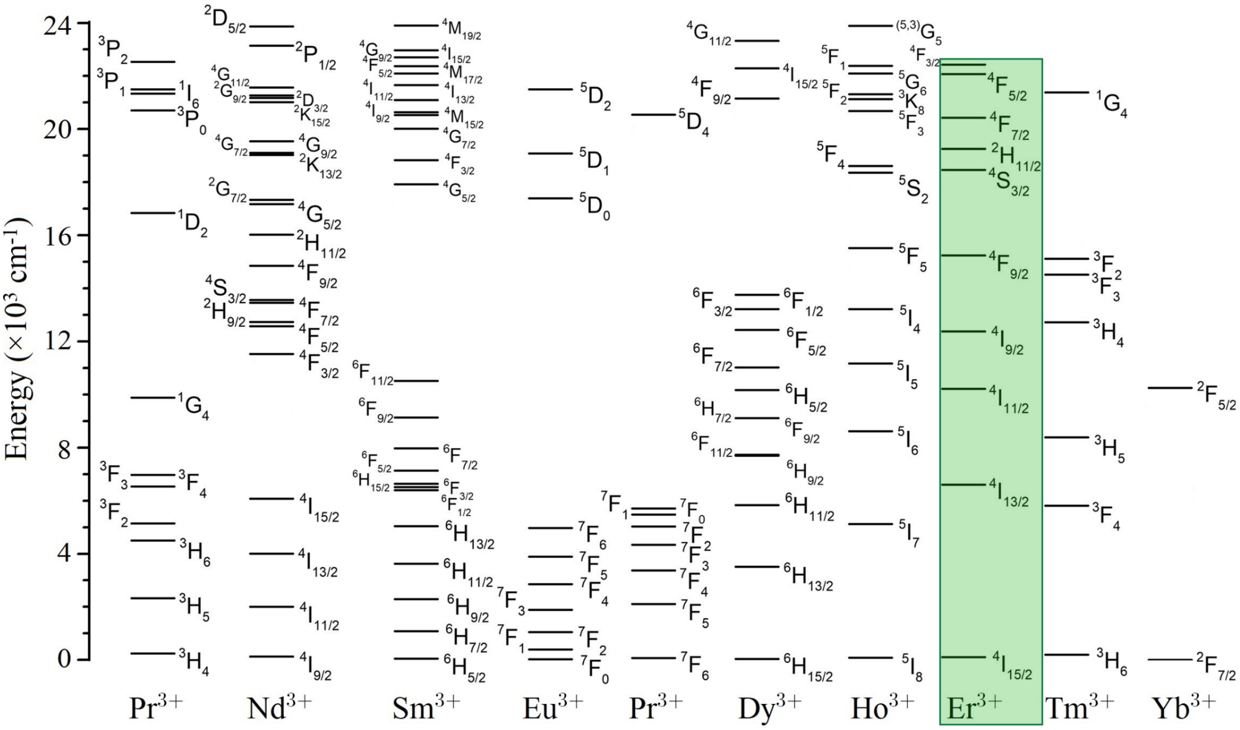

Figure 5 – RE ions energy-levels diagram. The column inside the green box corresponds to the energy levels of Er^{3+}.

Source: Adapted from KREIDT *et al.*, 2018.[52]

2.3 Surface Plasmons Polaritons

Plasmonics provides a unique platform for manipulating light by confining the electromagnetic field to sub-diffraction-limited regions. In recent years, there has been a growing interest in exploring the quantum properties of surface plasmons and developing plasmonic devices that operate at the quantum level. The potential of plasmonics to achieve strong coupling between light and emitting systems, such as quantum dots, RE ions, and nitrogen-vacancy centers, through highly localized fields opens up exciting opportunities for the quantum control of light. This field of research combines modern plasmonics with quantum optics is called "quantum plasmonics". It holds great promise in enabling efficient single-photon sources and advancing the quantum information processing field.[53]

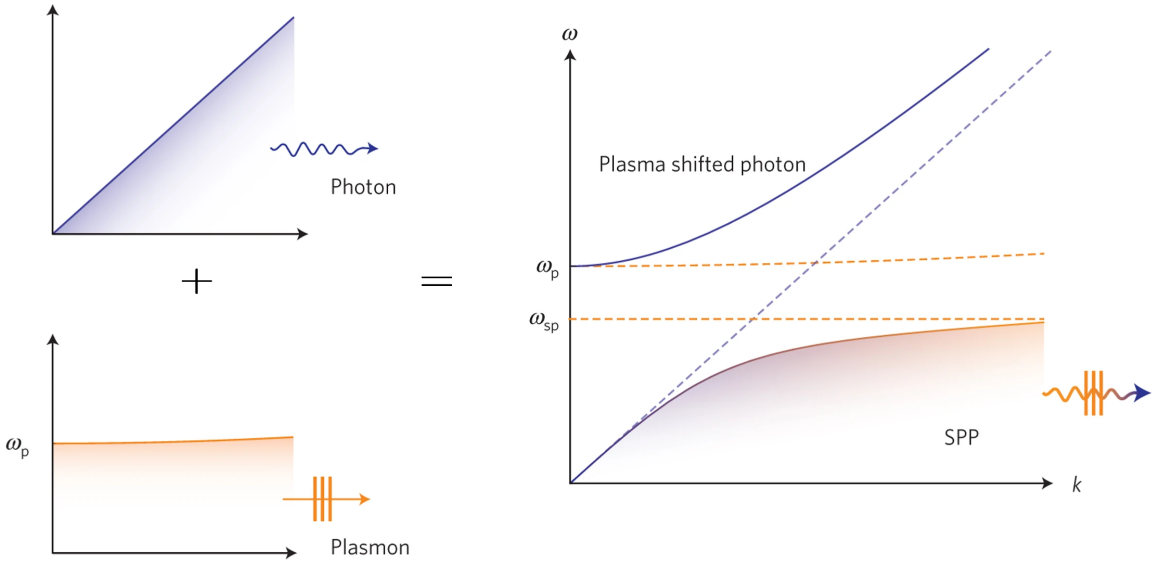

Figure 6 – Diagram of the coupling of a photon and a plasmon.

Source: Adapted from TAME *et al.*, 2013.[53]

A plasmon is a collective excitation of electrons in a metal that acts as a quantum of electromagnetic energy. It is created when light or other electromagnetic radiation is absorbed or scattered by the metal's free electrons, causing the electrons to oscillate in phase. Under certain conditions and at the metal-dielectric interface, the collective oscillations of electrons in the metal can propagate along the interface. These oscillations result in a localized and highly concentrated electromagnetic field called a surface plasmon polariton.[1,2] Surface Plasmons Polaritons play an important role in a variety of phenomena, including the enhancement of light-matter interactions, the formation of surface-enhanced spectroscopies (such as surface-enhanced Raman spectroscopy), the local density of states near metal nanostructures, the generation of hot electrons in metal nanostructures, and the confinement and control of light at the nanoscale.[34]

The quantization of plasmonics begins with the work of D. Pines, 1950[54] which provided the first model to quantify plasma waves in metals and reported that electrons in the conduction band are analogous to free electrons in a gas of electrons. J. J. Hopfield, 1958[55] defined the polariton as a light-matter joint state also presented a quantum model for the polarization field that describes the response of matter to light. The surface plasma wave (SPW) concept was proposed by Ritchie, 1957[56] and later Elson and Ritchie, 1971[57] used the approach presented by J. J. Hopfield, 1958[55] to provide a quantified description of SPW, the surface plasmon polariton (SPP). Figure 6 shows the coupling of a photon and a plasmon at the interface of a material with a negative dielectric function and one with a positive dielectric function leading to a splitting of the $(\omega - k)$ dispersion curves (solid lines) for the excitations, which form a plasma-shifted photon and an SPP as the joint state of light (photon) and matter (surface plasmon).[53] To explain the generation of the SPP, we can consider an incident electromagnetic wave at the interface between a dielectric and metallic medium as illustrated in Figure 7.a. The interest is in the incident and transmitted wave with transverse magnetic (TM) polarization, which means the magnetic field is parallel to the interface. The other case is the transverse electric polarization (TE), where the electric field is parallel to the interface.[58]

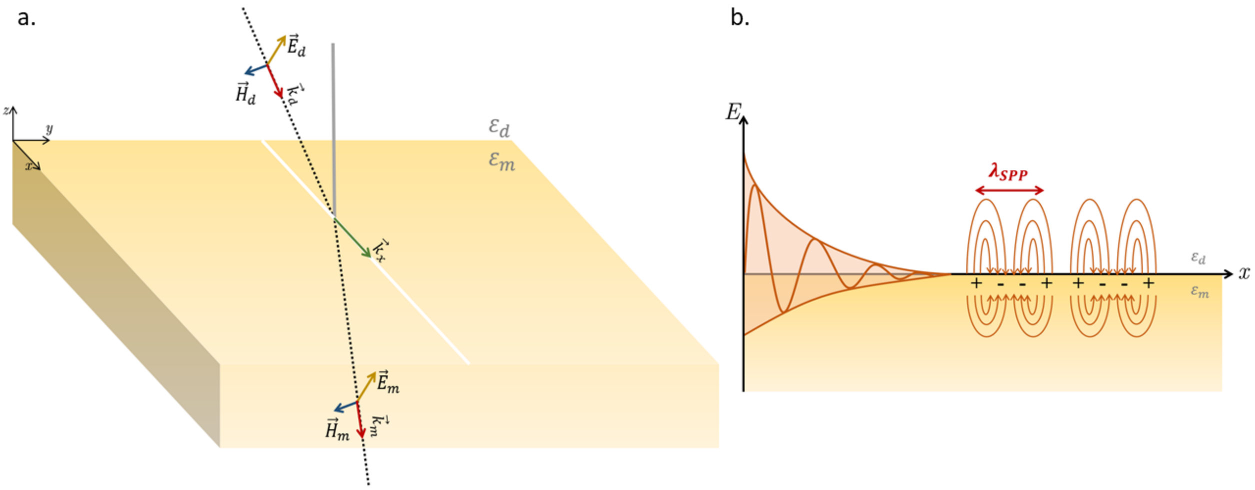

Figure 7 – a. Representation of an electromagnetic wave traveling from a dielectric medium with permittivity ε_d to a metallic medium with permittivity ε_m and b. Evanescent wave at the dielectric–metal interface in the axis x, where the SPP is generated

Source: Adapted from KUMAR *et al.*, 2016.[59]

The electric and magnetic field components in the dielectric medium ($z > 0$) can be written as follows:

$$\begin{aligned} E_{d,x} &= E_{d,x0}\mathrm{e}^{i\left(k_{d,x}x-\omega t\right)}\mathrm{e}^{-k_{d,z}z} \\ E_{d,z} &= E_{d,z0}\mathrm{e}^{i\left(k_{d,x}x-\omega t\right)}\mathrm{e}^{-k_{d,z}z} \\ H_{d,y} &= H_{d,y0}\mathrm{e}^{i\left(k_{d,x}x-\omega t\right)}\mathrm{e}^{-k_{d,z}z} \end{aligned} \tag{2.2}$$

and in the metallic medium ($z < 0$):

$$\begin{aligned} E_{m,x} &= E_{m,x0}\mathrm{e}^{i(k_{m,x}x-\omega t)}\mathrm{e}^{k_{m,z}z} \\ E_{m,z} &= E_{m,z0}\mathrm{e}^{i(k_{m,x}x-\omega t)}\mathrm{e}^{k_{m,z}z} \\ H_{m,y} &= H_{m,y0}\mathrm{e}^{i(k_{m,x}x-\omega t)}\mathrm{e}^{k_{m,z}z} \end{aligned} \tag{2.3}$$

Considering that the wave vector component parallel to the interface is conserved, i.e., $k_{d,x} = k_{m,x} = k_x$, and also at the interface, the boundary conditions are:

i. $H_{d,y} = H_{m,y}$, ii. $E_{d,x} = E_{m,x}$ and iii. $\varepsilon_d E_{d,z} = \varepsilon_m E_{m,z}$

Following the procedure detailed by J. Weiner, 2009,[60] which implies solving Maxwell's equations with these boundary conditions, obtain the dispersion relation, k_x:

$$k_x = k_{\mathrm{SPP}} = \frac{\omega}{c}\sqrt{\frac{\varepsilon_d \varepsilon_m}{\varepsilon_d + \varepsilon_m}} \tag{2.4}$$

where k_{SPP} is the propagation of the SPP and is valid for both real and complex ε_m. Further, the perpendicular component of the wave vector is:

$$k_{j,z} = \frac{\omega}{c}\frac{\varepsilon_j}{\sqrt{\varepsilon_d + \varepsilon_m}} \tag{2.5}$$

with $j = \{d, m\}$ for dielectric and metal region, respectively. Since k_{SPP} must be real; otherwise propagation would not occur, both the numerator and denominator inside the root square sign must be positive or negative. Furthermore, solutions near the interface lead to the existence of evanescent waves perpendicular to the interface (see Figure 7.b), and $k_{j,z}$ must be imaginary. Therefore, the only condition which satisfies the described statements is that both $\varepsilon_d \varepsilon_{\mathrm{m}}$ and $\varepsilon_d + \varepsilon_m$ must be negatives. With Equation 2.2, it can be seen that SPPs can be coupled back into the light if they encounter obstacles or defects, e.g., holes or corrugations while propagating along the surface. The coupling of light and SPP generates constructive or destructive interference. The latter is employed to obtain enhanced transmission in subwavelength apertures.[60]

The study of SPP bridges the gap between traditional optics and nanoscale phenomena, offering new avenues for manipulating light, enhancing light-matter interactions, and enabling novel applications in various fields of science and technology.[61–63]

3 METHODOLOGY

The idea of generating hybrid plasmonic systems arises from the need for strong coupling between the SPPs and the RE ions. In this dissertation, Er^{3+} doped glassy thin film systems deposited on gold nanoslits are proposed because these systems present greater proximity between SPP and RE ions. In this chapter, the methods used to fabricate these systems are presented, which consist of the synthesis of glasses, the fabrication of nanoslits in gold thin films using Focused Ion Beam (FIB) lithography, and the deposition of thin films using spin-coating.

3.1 Glass synthesis

The samples had the following chemical composition:

$$(60 - x)\%\ TeO_2 - 20\%\ ZnO - 10\%\ GeO_2 - 10\%\ Na_2O \text{ - } x\%\ Er_2O_3$$

where "x" represents the changes in the mole percentage (% mol) concentration of Er_2O_3 in the samples: ($x = 0.00,\ 0.001,\ 0.01,\ 0.05$ and 0.1). Glasses were labeled according to their chemical composition as TZGN$1000 \cdot x$. Table 3 shows the concentrations of the fabricated glass matrices.

Table 3 – Reagent concentration in the TZGN glasses (%mol)

Sample	Concentrations (%mol)				
	TeO_2	ZnO	GeO_2	Na_2O	Er_2O_3
TZGN0	60.00	20.00	10.00	10.00	0
TZGN1	59.999	20.00	10.00	10.00	0.001
TZGN10	59.99	20.00	10.00	10.00	0.01
TZGN50	59.95	20.00	10.00	10.00	0.05
TZGN100	59.9	20.00	10.00	10.00	0.1

Source: By the author.

The glasses were prepared using high-purity chemical reagents ($\geq$ 99.99%) in powder form obtained from Sigma-Aldrich. Reagents were weighed with a precision of ± 0.0001 gram using an electronic balance. Subsequently, the reagents were manually mixed and ground in an agate mortar to ensure homogeneity in the compound mixture. All these procedures were carried out inside a glovebox to minimize the presence of hydroxyl ions (OH^-) in the glass, which could result from moisture in the air.[64] The samples were made using the conventional melt quenching method (see Figure 8). Reagents were placed in a platinum crucible and introduced into a ceramic furnace at 300 °C (at a rate of 10

°C/min) for 30 minutes to remove any residual water molecules from precursor powders. Subsequently, the mixture was heated to 900 °C (at a rate of 10 °C/min) and melted in an induction furnace. A high-purity oxygen flow (5N) of 0.5 L/minute was injected during the melting process. The molten glass was poured into a preheated mold and annealed at 290 °C for 300 minutes in a muffle furnace. Finally, the glass was slowly cooled to room temperature (at 1 °C/min). This slow cooling process is essential to relieving mechanical stresses caused by melting and cooling, thereby preventing the glass from breaking during subsequent cutting and polishing procedures. The fabricated glasses were polished to a thickness of approximately 2.5 mm.

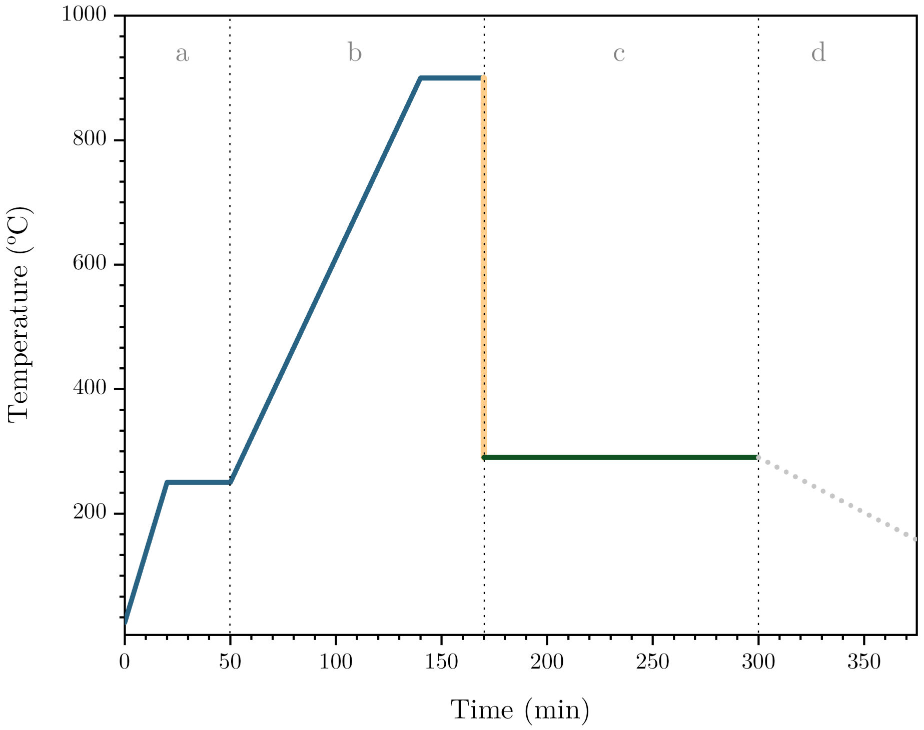

Figure 8 – Step-by-step glass fabrication process: a. The reagents were subjected to a 30-minute heat treatment at 300 °C in a ceramic furnace to eliminate water molecules. b. The reagents were melted for 30 minutes at 900 °C in an induction furnace. c. The resulting molten glass was subjected to a 300-minute thermal treatment at 290 °C in a muffle furnace. d. Finally, the furnace was allowed to return to room temperature at the end of the specified heat treatment time.

Source: By the author.

It should be mentioned that during the melting step, the introduction of oxygen gas (O_2) flow into the furnace was necessary to prevent the reduction of Tellurium to its metallic form and the subsequent recombination of oxygen with Tellurium, which could result in an opaque coloration of the glasses and compromise their optical quality. The synthesis of the glasses was carried out at the facilities of the Centre d´Optique Photonique et Laser, Universitè Laval, Canada.

3.2 Fabrication of nanostructures by lithography

Focused ion beam (FIB) lithography is a nanofabrication technique used in the microelectronics and nanotechnology industry. It consists of using a highly focused ion beam to sculpt or modify the structure of materials on a nanometric scale. Unlike other lithography techniques, such as optical or electron beam lithography, FIB offers higher resolution and the ability to perform direct three-dimensional modifications on samples. The fabrication of nanostructures in metallic films by FIB offers great versatility and allows the creation of complex and personalized patterns.[65] The FIB lithography process involves the following steps:

- Generation of the ion beam: An ion beam, in our case gallium metal in a liquid state (Ga^+)), is generated by an ionization process. Figure 9.a shows the FIB lithography system.
- Ion-beam focus: The ion beam uses electrostatic lenses, allowing for high resolution and small beam diameter.
- Scan and write: The ion beam is scanned over the sample surface in a predetermined pattern. During this process, the ions interact with the material and can perform various actions, such as removing material, depositing additional material, or changing the material's properties at the nanoscale level. Figure 9.b shows the processes involved in FIB lithography.
- Control and monitoring: During the writing process, it is essential to monitor by means of SEM and control various parameters such as ion beam current, ion energy, exposure time, and scan position. These parameters influence the precision and quality of the fabricated structures.

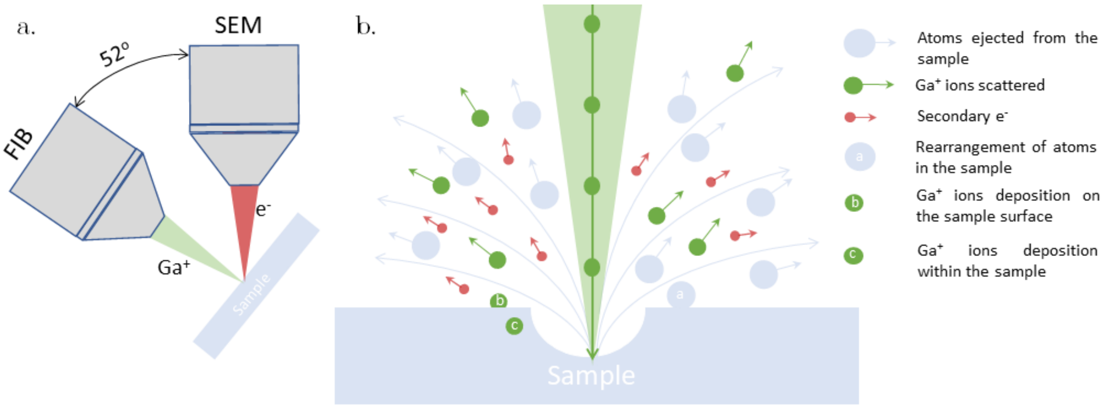

Figure 9 – FIB dual beam system diagram.

Source: Adapted from FRIEDESEN *et al.*, 2017.[65]

In this dissertation, a 100 nm gold (Au) film was deposited on the Si substrates by thermal evaporation using the Bal-Tec model BAE 250 system at 1000 °C (the Au melting point). Before the evaporation process, a vacuum of less than 10^{-6} mbar had to be made inside the chamber. The Au films were milled with an FEI-FIB Quanta 3D 200i using gallium ions (Ga^+, at 30 keV) to obtain nanoslits that form a plasmonic nanostructure. Figure 10 below shows the SEM images of the nanoslits composed of 100 nm wild slits (etched on the Si substrate) 20 μm long and separated by 1000 nm that form a square 20×20 μm^2. The fabrication of the nanostructures was carried out at the São Carlos Institute of Physics, University of São Paulo, Brazil.

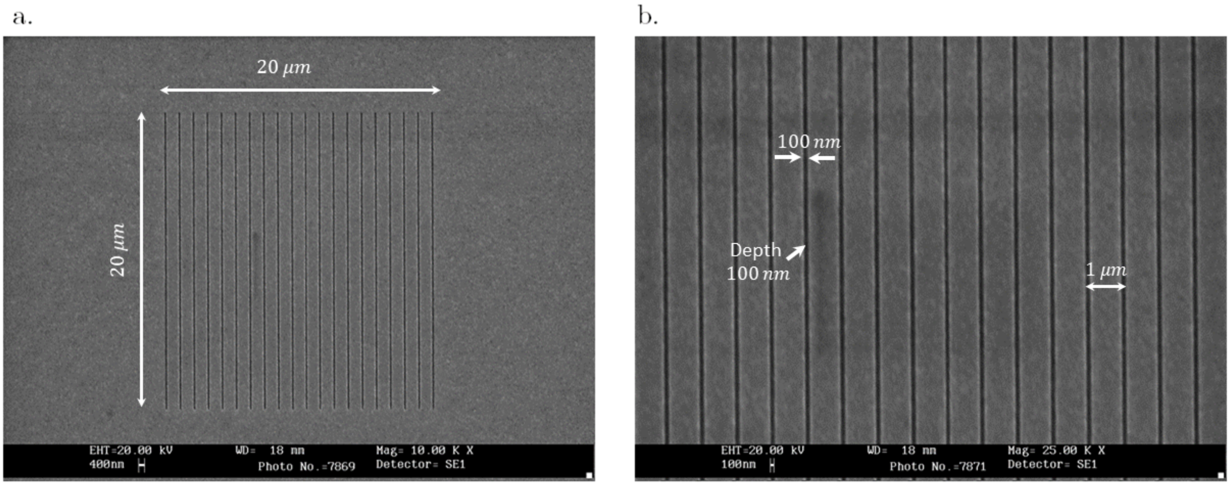

Figure 10 – SEM image of nanoslits.

Source: By the author.

3.3 Thin films fabrication

Most techniques for depositing thin films are based on vacuum technology, including pulsed laser deposition,[66] magnetron sputtering[67] and chemical vapor deposition,[68] but it has great limitations due to cost and scalability terms.[69] However, the spin coating technique has substantial advantages due to its simplicity, relatively inexpensive equipment, and less material loss compared to vapor deposition. Thin layers can be deposited quickly and easily, and novel results can be obtained with this technique.[70]

The fabrication process of the thin film was conducted as follows: Initially, the glass was ground to a fine powder using an agate mortar for 1 hour. Subsequently, the glass powder was placed in 14 mL vials with 2 mL of 2-propanol alcohol and 4.5 mL of zirconia yttria oxide spheres with a diameter of 2 mm. The vials were then placed in a rotational mill (see Figure 11.a) with a rotation speed of 35 rpm for 200 hours.[71]

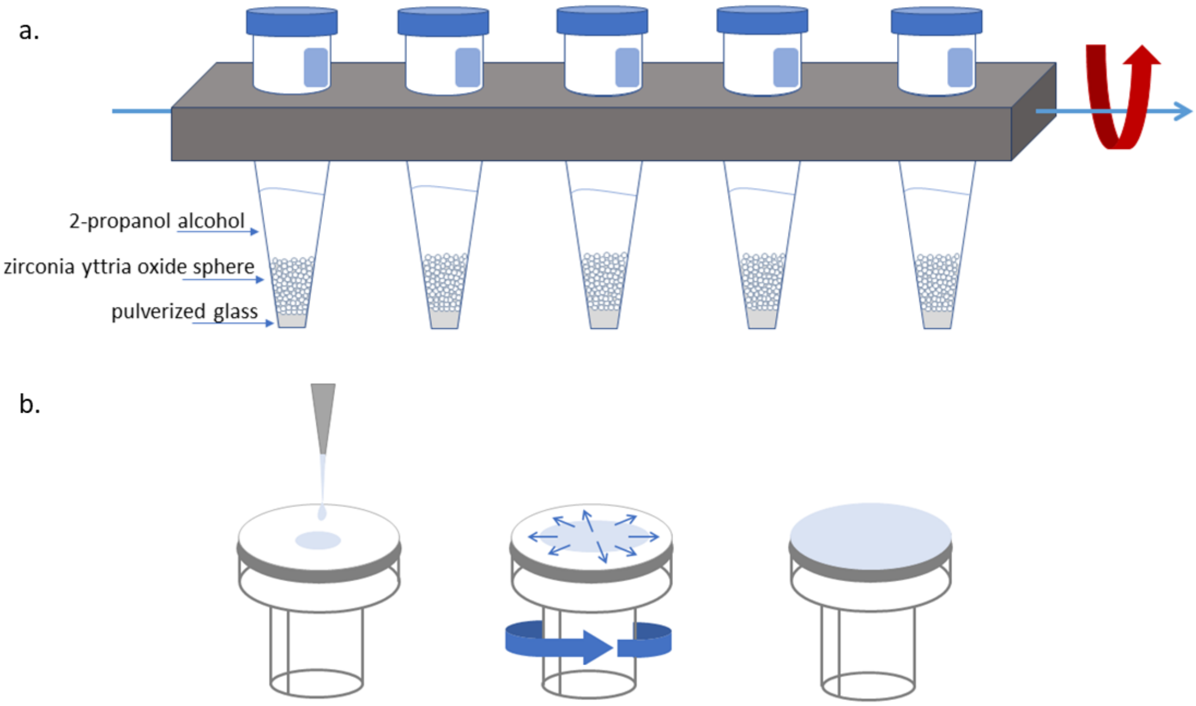

Figure 11 – a. Scheme of rotational milling equipment and b. Scheme of step-by-step spin-coating deposition scheme.

Source: Adapted from CLABEL *et al.*, 2020.[72]

The solution to be deposited was based on glass nanoparticles (nanoglass) and polymethylmethacrylate (PMMA), but the PMMA needed to dissolve, for which anisole was used, which played the role of solvent. The first step is to weigh 50 ml of anisole and calculate 3% of the weight, which will be the amount of PMMA to dissolve in the anisole. Then 55 mg of nanoglasses were weighed and mixed with anisole in a borosilicate beaker. This mixture was heated in a water bath at 60 °C inside ultrasonic equipment for 30 minutes to disaggregate and homogenize the nanoglasses in the anisole. Subsequently, the mixture was transferred to a magnetic stirrer, PMMA was slowly added for 15 minutes, and it was left to mix for 30 minutes at 60 °C. The substrate used for the deposition of thin films was pure silicon (Si), as it does not exhibit luminescence under an excitation of 980 nm.

The spin coating technique consists of depositing a solution on a substrate rotating at a high angular speed (see Figure 11.b). During rotation, the solution is spread with a micropipette on the substrate that is fixed by an aspiration to a rotating stage producing the thin film, which is produced due to the dispute of the adhesive forces of the solution and the substrate with the centrifugal force.[73] Fluid viscosity, speed of rotation, and acceleration of the turntable are the two main parameters controlling the thin film's thickness.[74]

The fabrication of thin films was carried out in a clean room, which has a continuous flow of clean air and a control system of temperature (20-22 °C) and humidity (40-65%). The deposition was performed on a Karl-Suss model SM 240-300 photoresist spinner. 60 μL of the solution was collected and deposited on the substrate with a micropipette. It was prepared in two rotations: the first at 800 rpm for 10 s to disperse the solution on the substrate and the second speed was 1500 rpm for 60 s to homogenize the film and obtain a lower thickness. The thin film manufacturing methodology was based on previous work in the research group, which has already been verified and published in indexed journals.[75,76] The product obtained from this process was a hybrid plasmonic system consisting of a PMMA thin film embedded with nanoglasses doped with Er^{3+} ions deposited in Au nanoslits. A representative scheme is shown in Figure 12. The fabrication of the thin films was carried out at the São Carlos Institute of Physics, University of São Paulo, Brazil.

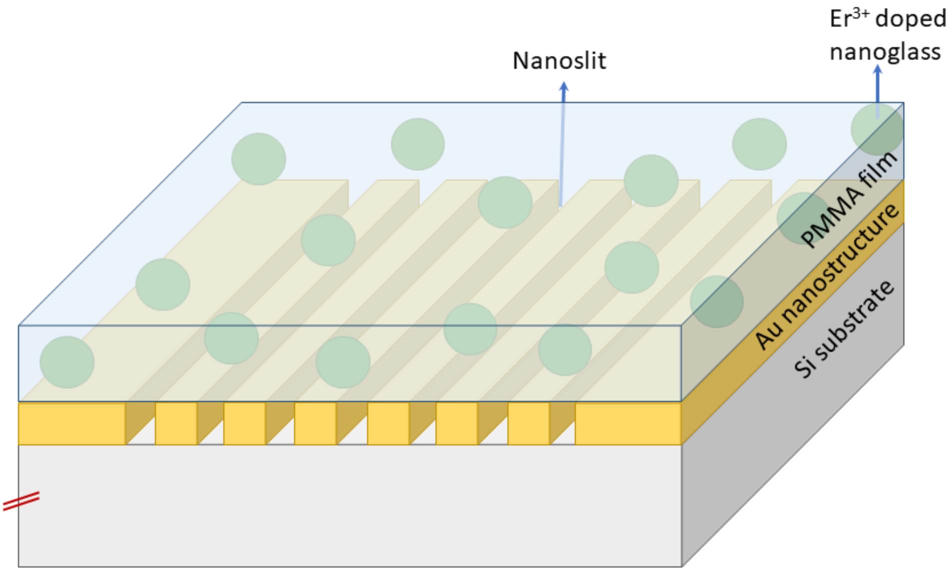

Figure 12 – Scheme of hybrid plasmonic system.

Source: By the author.

3.4 Characterization techniques

3.4.1 The concentration of RE ions

To determine the concentration of Er^{3+} ions in each sample, it is necessary to know the density of the glasses, which was calculated using Archimedes' principle, measuring the volume displaced when each sample is immersed in water and obeys the following relationship:

$$\rho = \frac{m}{m - m'} \rho_{H_2O} \tag{3.1}$$

where m and m' are the masses of glass measured in air and water, respectively, and ρ_{H_2O} is the density of distilled water, which depends on temperature. Measurements were made in an analytical balance of Mettler Toledo AG285 model with precision in grams of ± 0.0001, and the temperature of the distilled water was 23.0 ±0.2 °C. Now, to measure the concentration of Er^{3+} ions, the following expression applies:

$$N_0 = \%C_{Er}\frac{2N_A\rho}{M_T} \tag{3.2}$$

where $\%C_{Er}$ is the concentration in %mol of Er_2O_3, N_A is the Avogadro number, ρ is the density of the glasses and M_T is the total molar mass. The measurements were made at the facilities of the São Carlos Institute of Physics, University of São Paulo, Brazil.

3.4.2 X-ray diffraction spectroscopy

Measurements were made on a Rigaku X-ray diffractometer, Ultima IV model, with a Cu Kα radiation source (λ = 0.15418 nm) in a sweep mode with an angle of 1.5°, the step size was 0.020/second and the diffraction angle 2θ covered the range from 10 to 100°. The measurements were made at the facilities of the São Carlos Institute of Chemistry, University of São Paulo, Brazil.

3.4.3 Fourier transform infrared spectroscopy

Measurements were made on a Shimadzu model IRAffinity 1 FTIR spectrophotometer, using the attenuated total reflection technique, which is especially useful for analyzing samples that cannot be analyzed for transmission due to opacity or inhomogeneity in the sample. The measurements were made at the facilities of the São Carlos Institute of Chemistry, University of São Paulo, Brazil.

3.4.4 Raman spectroscopy

Measurements were made on a Horiba model LabRaman HR Evolution Raman spectrometer, using a 633 nm He-Ne laser as an excitation source with controlled power to avoid any possible heating effect; additionally, ultralow-frequency filters were used to be able to collect data of low wavenumbers (<15 cm^{-1}), where information is found on boson peaks in vitreous materials. The measurements were made at the facilities of the Department of Physics, Federal University of São Carlos, Brazil.

3.4.5 Refractive index measurements

The refractive index measurements were made with the prism-coupling technique (with a refractive index of 2.8654) in a Metricon M-Line 2010 spectrometer at three wavelengths of 532.0, 632.8, and 1538 nm, with transverse electrical (TE) and magnetic (TM) component polarizations. This equipment has a resolution of ± 0.0001. The data obtained fit the Sellmeier equation:

$$n^2 = 1 + \frac{A\lambda^2}{\lambda^2 - B} \tag{3.3}$$

where n is the refractive index, λ is the wavelength, and A (dimensionless) and B (nm^2) are experimentally determined Sellmeier coefficients.[77] The measurements were made at the facilities of the Ribeirão Preto Faculty of Philosophy, Sciences and Letters, University of São Paulo, Brazil.

3.4.6 UV-VIS-NIR absorption spectroscopy

Measurements were made on a PerkinElmer Lambda 1050 model spectrophotometer, capable of characterizing materials concerning optical transmission and reflection in the regions between ultraviolet (175 nm) and visible/near-infrared (3300 nm). The equipment has three detectors: Photomultiplier R6872 for high energy in the UV/VIS range, an InGaAs detector cooled by Peltier in the range of 860 - 1800 nm, and a PbS detector in the range of NIR (1800 - 3300 nm). The measurements were made at the facilities of the Department of Physics, Federal University of São Carlos, Brazil.

3.4.7 Luminescence spectroscopy and Up-conversion

At room temperature, measurements were made on a Horiba photoluminescence microspectrometer, model iHR320. The excitation wavelength (λ_{exc}) was 980 nm, and a 10x microscope objective lens was used to focus the laser at a fixed point with a diameter of 60 μm. The Up-conversion emission intensity (I_{Uc}) is proportional to the nth power of the IR excitation intensity (I_{exc}), so:

$$I_{Uc} \propto I_{exc}^n \tag{3.4}$$

where n is the number of IR photons involved in the population inversion process of each Up-conversion emission band and is determined by a linear fit, where n must be an integer. The power ranged from 40 to 200 mW. The measurements were made at the facilities of the São Carlos Institute of Physics, University of São Paulo, Brazil.

3.4.8 Lifetime measurements

Emission decay measurements to obtain lifetimes were obtained on a Horiba Fluorolog 3 spectrofluorimeter equipped with a double monochromator of visible emission using an uncooled Hamamatsu R982P photomultiplier as a detector. In the infrared region, the detector used was a Hamamatsu H10330-75 photomultiplier, and the excitation source was a laser operating at 980 nm pulsed mode. The measurements were made at the facilities of the Ribeirão Preto Faculty of Philosophy, Sciences and Letters, University of São Paulo, Brazil.

3.4.9 Scanning electron microscopy

The measurements were made in a Leo model 440 scanning electron microscope to study the grain size distribution of the nanoglasses. As an instrument requiring a high vacuum, only solid samples are analyzed. The results were analyzed in ImageJ software. The measurements were made at the facilities of the São Carlos Institute of Physics, University of São Paulo, Brazil.

3.4.10 Atomic force microscopy

The measurements were made in a Bruker model dimension icon NanoScope V atomic force microscope. The morphology, texture, and thickness of the thin films were studied. The data obtained were analyzed with the NanoScope Analysis software. The measurements were made at the facilities of the São Carlos Institute of Physics, University of São Paulo, Brazil.

3.4.11 Scanning confocal fluorescence microscope

Measurements were made on an Invert Zeiss LSM 780 multiphoton laser scanning confocal fluorescence microscope (LSCF) with a spatial resolution of 300 nm and 32 high-sensitivity photodetectors for spectral images. The excitation source is a Ti:Sapphire laser tuned at 980 nm linearly polarized and in a configuration perpendicular to the samples to measure. The measurements were made at the facilities of the São Carlos Institute of Physics, University of São Paulo, Brazil.

4 GLASS CHARACTERIZATION RESULTS

Glasses have interesting properties and are technologically relevant applications in the areas of health,[20] energy conversion[21] and photonics.[23] Developing these and other applications requires a deep understanding of glasses' optical and structural properties. This knowledge facilitates the design and optimization of advanced optical and photonic devices. In this chapter, we will present detailed results of the optical and structural characterization of Er^{3+}-doped TZGN glasses used for nanoparticle fabrication, establishing the foundations for future innovative research and technological applications.

4.1 Characterization of glasses

After synthesis, the glasses were processed to achieve an average thickness of 1.5 mm.

Figure 13 – Samples of TZGN glasses.

Source: By the author.

Rare-earth ions concentration

The data obtained for the density of each sample and its corresponding rare earth concentration are presented in Table 4.

Table 4 – Sample labels, density, total molecular weight and concentration of Er^{3+}

Sample	Density g/cm^3	Total molecular weight (g/mol)	Concentration (10^{20} ions/cm^3)
TZGN0	5.123	128.695	0
TZGN1	5.121	128.698	4.793×10^{-3}
TZGN10	5.127	128.718	4.797×10^{-2}
TZGN50	5.117	118.345	2.604×10^{-1}
TZGN100	5.123	118.456	5.219×10^{-1}

Source: By the author.

X-ray spectroscopy

The amorphous materials have diffraction patterns but do not have Bragg diffraction from the lattice planes, resulting in typical noncrystalline behavior.[78] To confirm this behavior, the XRD patterns are shown in Figure 14, from which is clear the absence of three-dimensional lattice periodicity and long-range atomic arrangements in the glass samples. The XRD spectrum shows a peak that stands out around 30° for all our samples, which indicates the presence of short-range order in the glasses, caused by the crystalline phase of TeO_2 located close to that position.[79]

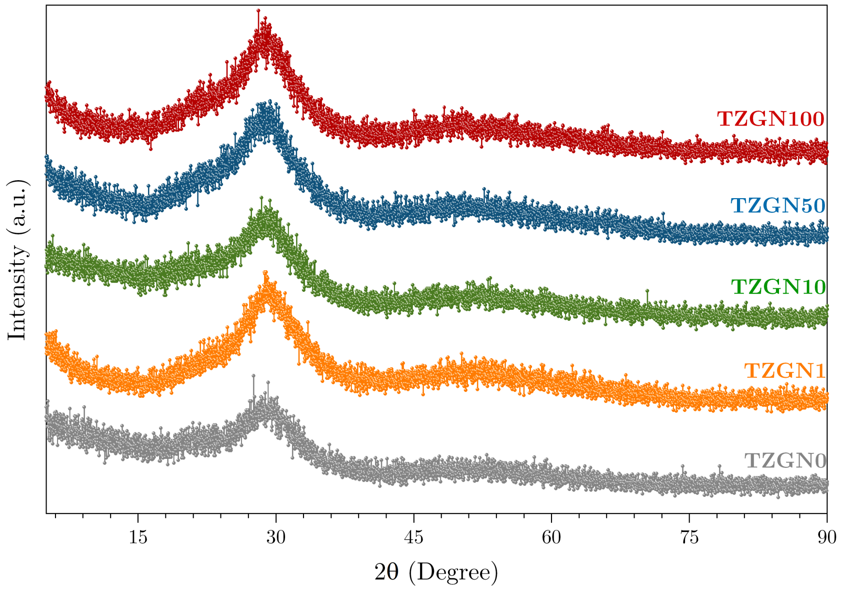

Figure 14 – X-ray diffraction spectra of TZGN glasses.

Source: By the author.

Fourier transform infrared spectroscopy

The transmission spectra of the glasses in the infrared region are shown in Figure 15. The transmittance of the glasses is approximately 80%, indicating good transmission in the mid-infrared region. The absorption edge of the multiphonon is indicated by the dashed cherry line located around 1840 cm^{-1}. The peaks observed in the yellow region of the FTIR figure (around 2360 cm^{-1}) correspond to the absorption region of the carbonyl functional groups (C=O) on the glass surface. The peaks observed in the orange region of the FTIR figure (around 2915 cm^{-1}) correspond to the absorption region of the functional groups of aliphatic hydrocarbons (CH) present in organic molecules on the surface. The red region (the valley ranging from 3500 to 3000 cm^{-1}) corresponds mainly to the stretching band of hydrogen bonds. This band may be present in tellurite glasses due to hydroxyl (-OH) groups in the glass lattice structure. However, Figure 15 shows a weakly pronounced band, indicating that the concentration and distribution of -OH groups are not very intense in the glassy structure. This could be attributed to the preparation of glasses in the induction furnace, which likely removed a significant amount of H_2O molecules during the melting of chemical reagents.[80]

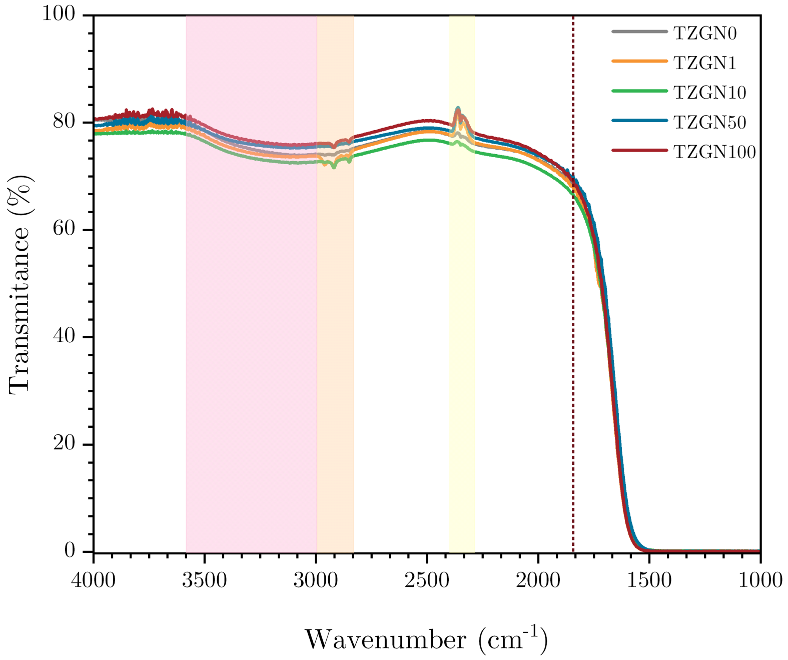

Figure 15 – FTIR spectra of TZGN glasses

Source: By the author.

Raman spectroscopy

Figure 16.a shows the Raman spectra of the TZGN glasses in the spectral range of 200 to 1200 cm^{-1}. Among the spectral components that comprise the Raman profile, the last visible peak of the Raman spectra in glassy materials is related to the phonon energy (E_{ph}) and in our case study, a shift towards a higher wavenumber. In the case of our glass samples, Er_2O_3 doping can affect the phonon energy due to the interaction between Er^{3+} ions and glass atoms. Furthermore, Er^{3+} ions can act as centers of phonon scattering, which means they can slow down phonons and increase their energy.[81] Furthermore, the presence of Er^{3+} ions can affect the structure of the glassy lattice, leading to increased stiffness and changing the frequency and amplitude of phonon vibrations, increasing phonon energy[82]. The cyan region in Figure 16.a highlights the E_{ph} region. Furthermore, Figure 16.b exhibits a sudden rise in the non-bridging oxygen (NBO) areas with increasing Er^{3+} ion concentration. This indicates a progressive modification in the TeO_2 structure coordination (4 $\rightarrow$ 3+1 $\rightarrow$ 3), resulting from the disruption of Te-O bonds. This leads to structural alterations in the glassy structure and the formation of NBO as a consequence of the incorporation of Er^{3+} ions.

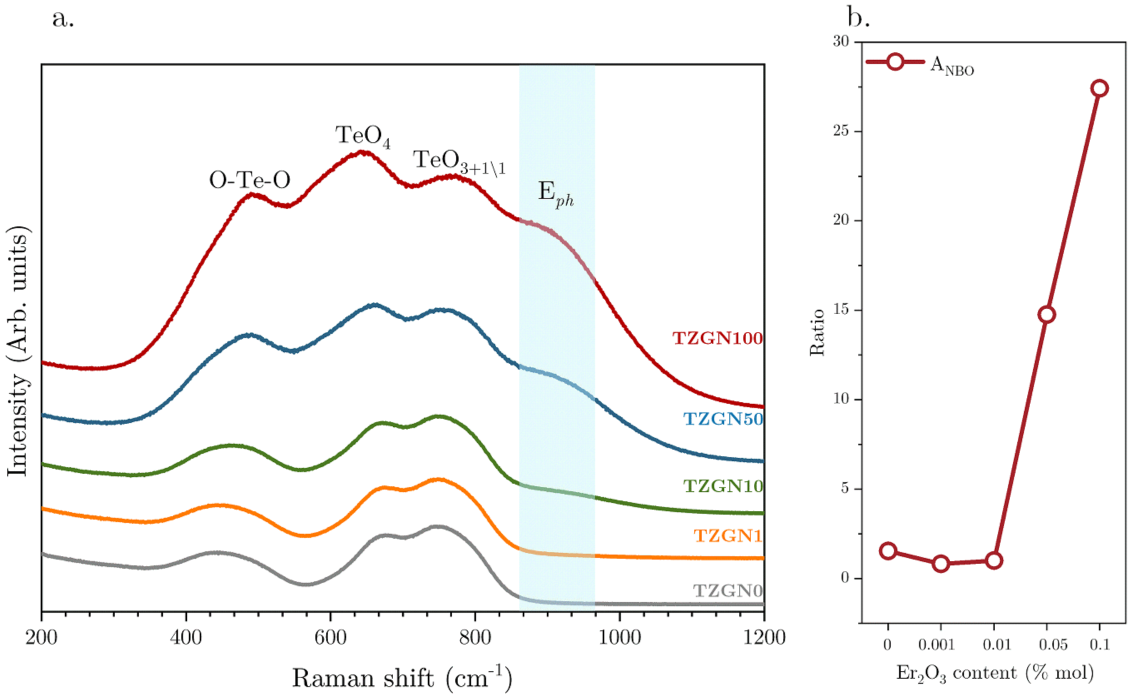

Figure 16 – a. Raman spectra of TZGN glasses. b. NBO areas

Source: By the author.

Measurements of refractive index

The results obtained from the measurements of the refractive index are reported and fit to the Sellmeir equation. The results are presented in Table 5.

Table 5 – Refractive index in function of λ (nm) of TZGN glasses.

Wavelength (nm)	Sample				
	TZGN0	TZGN1	TZGN10	TZGN50	TZGN100
532	2.0073	2.0064	2.0069	2.0068	2.0057
632.8	1.9823	1.9812	1.9814	1.9817	1.9815
1538	1.9338	1.9332	1.9343	1.9341	1.9330
A	2.7049	2.7024	2.7068	2.7063	2.7029
B (nm^2)	30431.043	30315.318	29980.607	30065.360	30144.210

Source: By the author.

The fit was optimal, with a value of $R^2 > 0.99$, and the Sellmeier coefficients A (dimensionless) and B (nm^2) were obtained. High refractive index values were obtained, taking silica glasses as a reference (>1.5).

UV-VIS-NIR Absorption Measurements

Figure 17 presents the absorption spectra of the samples in the 360 – 1150 nm region. The absorption bands corresponding to the electronic transitions from the ground state $^4I_{15/2}$ of the Er^{3+} to the excited states $^4G_{11/2}$, $^2H_{9/2}$, $^4F_{3/2}$, $^4F_{5/2}$, $^4F_{7/2}$, $^2H_{11/2}$, $^4S_{3/2}$, which are observed at wavelengths of 390, 408, 445, 450, 488, 522, 545, 653, 815, and 976 nm, respectively. The absorbance band in the infrared (IR) region around 1530 nm ($^4I_{15/2} \rightarrow {}^4I_{13/2}$) is illustrated in the inset of Figure 17.

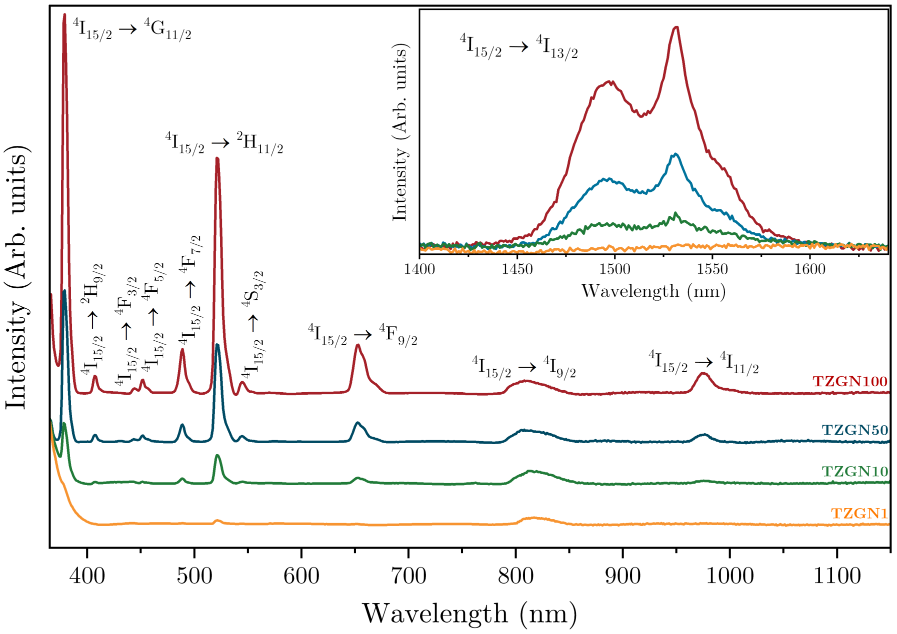

Figure 17 – Absorbance spectra of TZGN glasses. The inset shows the absorption in the NIR region, showing the $^4I_{15/2} \rightarrow {}^4I_{13/2}$ band around 1530 nm.

Source: By the author.

Based on the absorption spectra,[83] the direct and indirect band gaps were calculated using the Tauc-Meth model[84] and are presented in Table 6. The observed increase in direct and indirect band gaps with Er^{3+} ion content can be attributed to modifying the glass network and, consequently, the local field surrounding these ions. The indirect band gap is associated with misalignment between the conduction and valence bands, influenced by the phononic contribution of the matrix.[85] On the other hand, the Urbach energy suggests an increase in structural disorder, which is a consequence of increasing Er^{3+} doping and can be attributed to a lower packing efficiency.[86] An increase in the value of E_U was observed, indicating an increase in structural disorder of our glass samples due to the incorporation of Er^{3+} ions, leading to the breaking of Te-O bonds and subsequent alteration of the glassy structure.[64]

Table 6 – Direct and indirect bandgaps and Urbach energies of TZGN glasses.

Sample	Direct bandgap (eV)	Indirect bandgap (eV)	Urbach energy (eV)
TZGN0	3.481	3.125	0.164
TZGN1	3.182	3.134	0.173
TZGN10	3.484	3.173	0.178
TZGN50	3.492	3.193	0.182
TZGN100	3.510	3.197	0.193

Source: By the author.

Luminescence and up-conversion spectroscopy

Figure 18 shows the up-conversion spectra of the TZGN glasses excited at 980 nm and varying the excitation intensity (I_{exc}). Three emission bands were observed, centered at 520, 550 and 660 nm, which corresponds to the Er^{3+} band: $^2H_{11/2} \rightarrow ^4I_{15/2}$, $^4S_{3/2} \rightarrow ^4I_{15/2}$ (green region) and $^4F_{9/2} \rightarrow ^4I_{15/2}$ (red region), respectively.

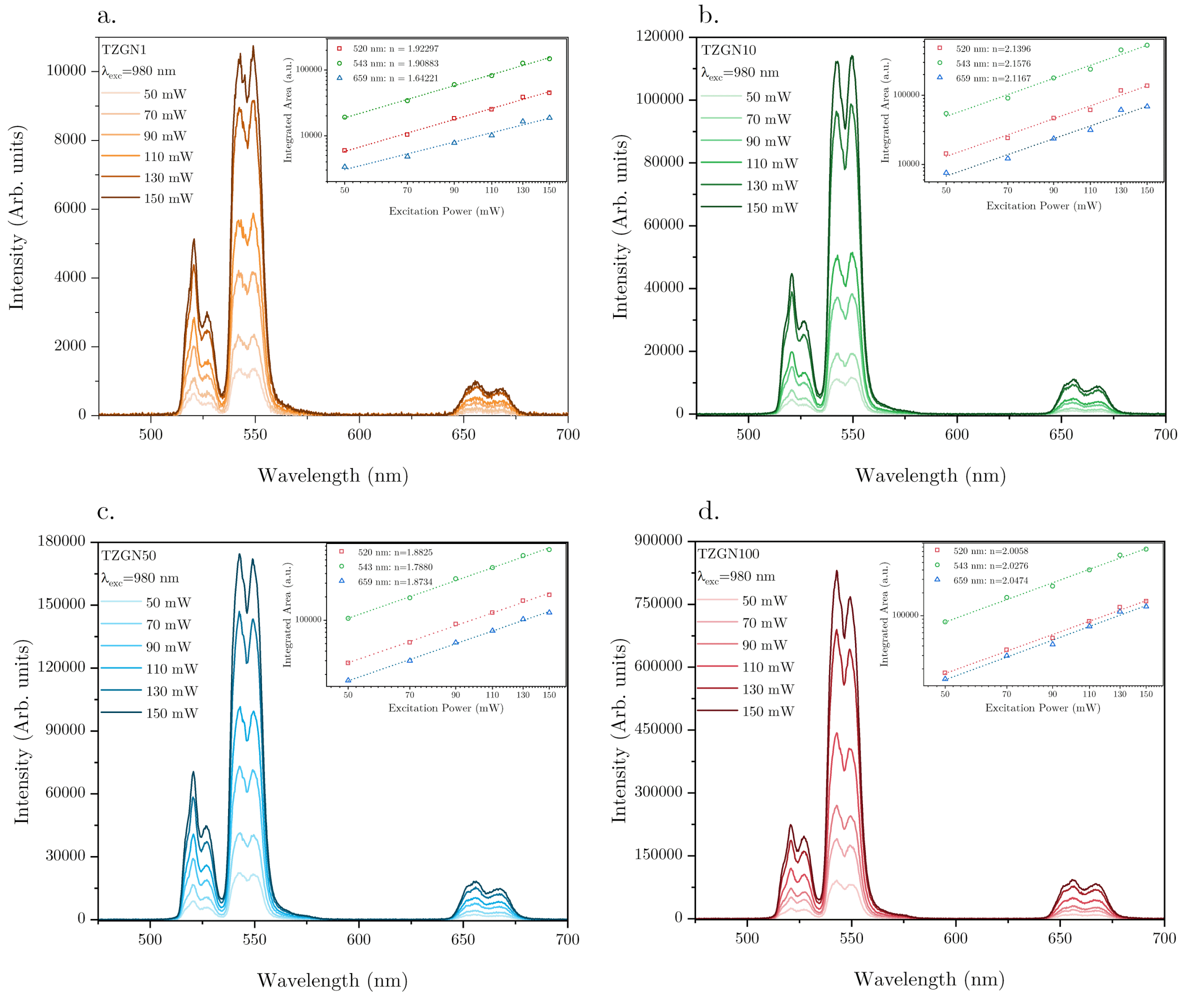

Figure 18 – Up-conversion of TZGN glasses

Source: By the author.

The emission in the green region is predominant in all samples. Subsequently, the emission in the red region is much lower than in the green region, and this trend remains constant in all samples. Therefore, it is suggested that the crystal field potential generated by the germane-tellurite host favors the green rather than the red emission of Er^{3+} ions.[87] On the other hand, in the insets of Figure 18, the number of IR photons (n) involved in each U_c process was reported, obtained from the slope of the function I_{U_c} versus I_{exc}. Since n has to be an integer, it is rounded to two: the photons involved in the bands centered at 520, 550, and 660 nm. The energy level diagram proposed in Figure 19 is based on the quadratic dependence of the pumping power.[88]

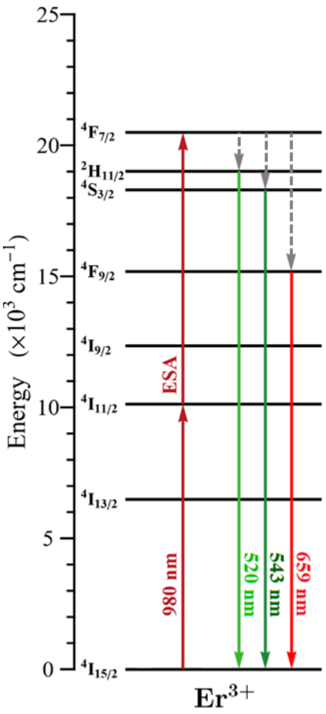

Figure 19 – Simplified energy level diagram with the possible transition pathways for the Er^{3+}-doped TZGN glasses.

Source: By the author.

Figure 20.a shows the emission spectra under 980 nm excitation, showing the band centered at 1530 nm corresponding to the $^4I_{13/2} \rightarrow {}^4I_{15/2}$ transition. No change in the position of the peak was observed. The energy level diagram is presented in Figure 20.b, it is observed that a 980 nm photon is involved (solid cherry arrow) that excites the $^4I_{11/2}$ state, then through non-radioactive transitions (dotted gray arrow), it decays to the $^4I_{13/2}$ state, to finally return to the ground state (solid brown arrow) emitting an IR photon of 1532 nm.

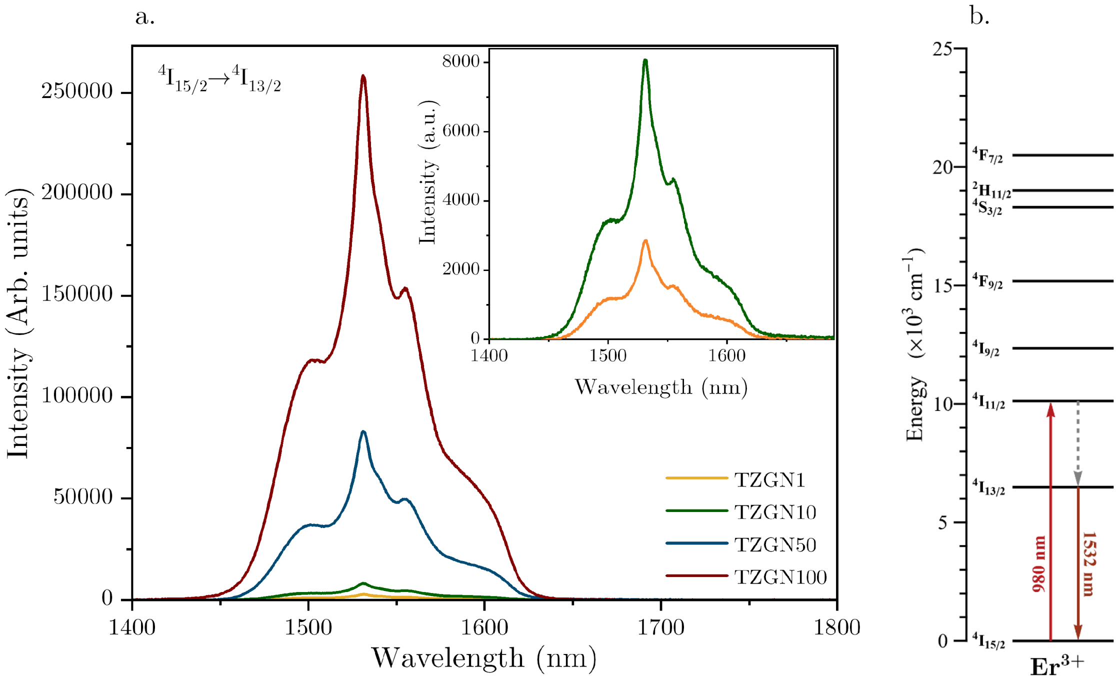

Figure 20 – Emission of TZGN glasses excited at 980 nm in NIR region (1530 nm)

Source: By the author.

The increase in FWHM emission in the NIR region increases with the Er^{3+} ion concentration. This may be related to the ion-ion interaction since at higher concentrations of Er^{3+} ions, the probability of energy transfer between neighboring ions increases. This would generate the superposition of the electronic states due to the proximity between the ions and give rise to the increase of the FWHM.[89] Furthermore, the increase in Er^{3+} ions also generates local variations in the matrix environment. These variations can lead to variations in the local electric fields and in interactions with Er^{3+} ions, which in turn can amplify the FWHM.[87] The results also suggest that the local crystal field generated by the TZGN glasses helps to broaden the Er^{3+} emission band to 1530 nm, indicating that our glasses are good candidates for IR amplifiers.[90]

Lifetime Measurements

The radiative lifetime measurements of the $^2H_{11/2}$ (526 nm), $^4S_{3/2}$ (546 nm) and $^4I_{13/2}$ transitions (1530 nm) to $^4I_{15/2}$ are reported in Figure 21. The curves were fitted to the function ExpDec1. It was impossible to measure the lifetimes of the TZGN1 sample due to its low amount of Er^{3+} (0.001 %mol) and because the accuracy of the equipment is not sensitive enough to detect this amount of doping. In the green spectral region, the observed variation in a radiative lifetime can be attributed to defects in the glass generated by the increase in Er^{3+} ions. These defects can serve as non-radiative absorption centers, competing with the radiative emission of Er^{3+} ions by absorbing their energy. As a result, the radiative lifetime decreases. In the case of the transition from the NIR region, the increase in the concentration of Er^{3+} ions in the glass can lead to an increase in the radiative lifetime because as the concentration of Er^{3+} ions in the glass increases, the ions may interact with each other, which can increase the efficiency of radiative emission. Furthermore, in the NIR region, the radiative emission of Er^{3+} ions is less susceptible to the influence of defects in the glass. Consequently, this leads to a higher radiative emission efficiency than other spectral regions.

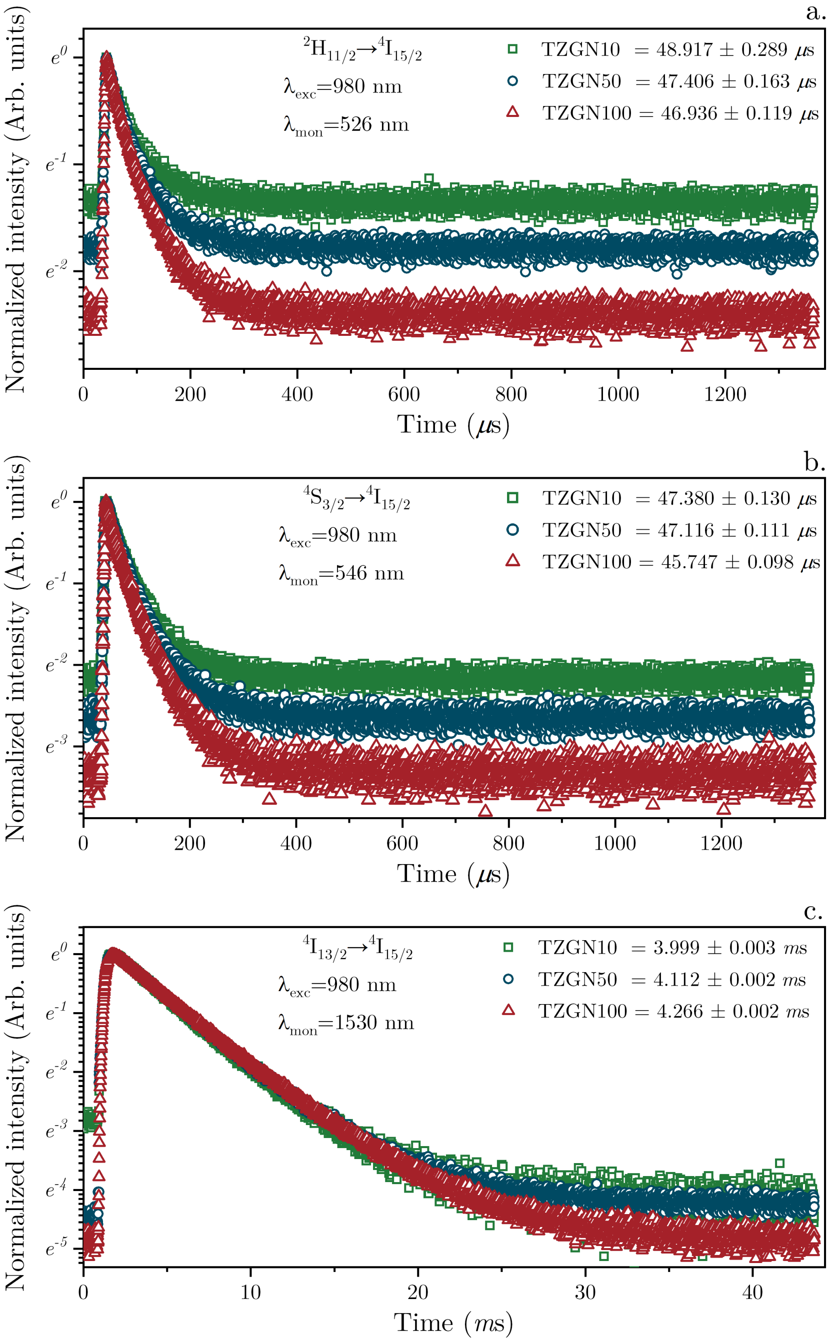

Figure 21 – Lifetime decay curves of TZGN glasses

Source: By the author.

5 PLASMONICS NANOSTRUCTURES RESULTS

In this final chapter, we will present the results of the morphology and the optical properties of nanoglasses deposited on gold nanoslits. The methodology for preparing the gold nanostructures and nanoglasses thin film was described previously in Chapter 3. Initially, results of the morphology of thin films obtained from SEM and AFM were used to determine the size distribution, shape, and homogeneity. The optical properties (spectral and lifetime) for the visible Er^{3+} transitions will be presented in the second section using confocal imaging microscopy. The visible regions transition lifetime measurements were performed using the Fluorescence Lifetime Imaging (FLIM) technique and will be presented in the third section. The microluminescence mapping technique was used to study the interactions between SPPs and Er^{3+} ions in the NIR regions. The results show a clear interaction of SPP with RE ions near the nanostructures. In all results that will be present in this chapter, the nanoglasses were obtained from the TGZN5 glass.

5.1 Thin film morphology

The morphology (size and homogeneity) of the thin films was assessed first through SEM measurements (see Figure 22.a). The average size of the nanoparticles incorporated within the PMMA matrix was approximately 300 nm (refer to Figure 22.b).

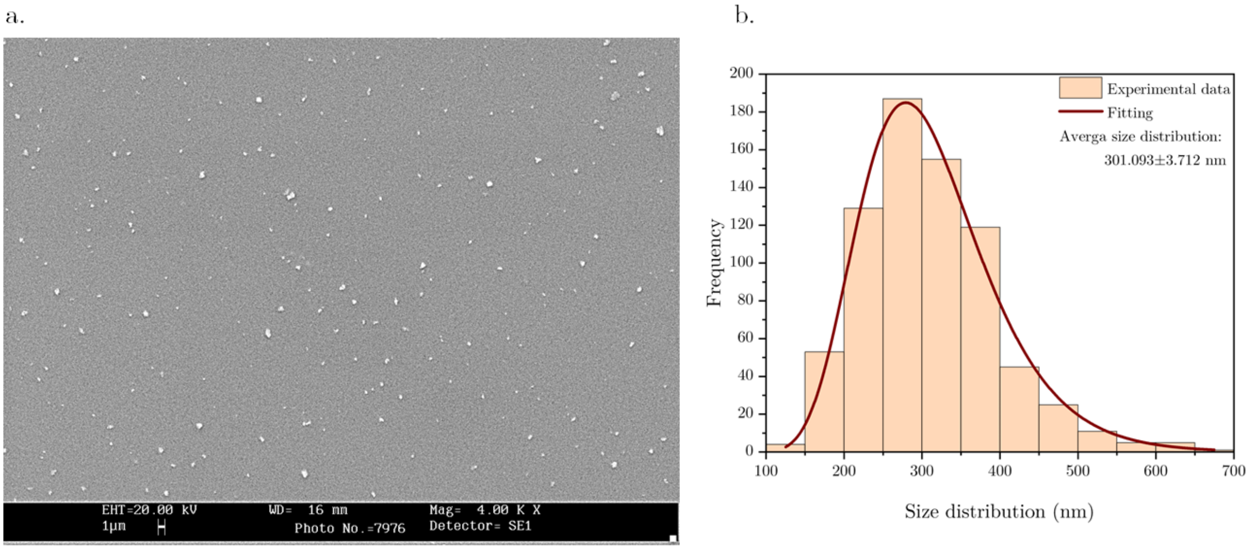

Figure 22 – a. SEM image of the thin film surface; b. Size distribution histogram of the lateral dimensions of the NPs obtained from the SEM image

Source: By the author.

Figure 23.a shows the SEM image of the thin films on the nanostructure. The Au nanostructure comprised 20 nanoslits with a width of 100 nm and spaced every 1 μm, forming a 20×20 μm^2 square. The lighter dots in the Figure indicate the nanoglasses immersed in the PMMA film. The image 23.b shows details of nanoparticles where it is possible to observe the irregularity in the form due to the methodology used in the manufacture (mechanical grinding).

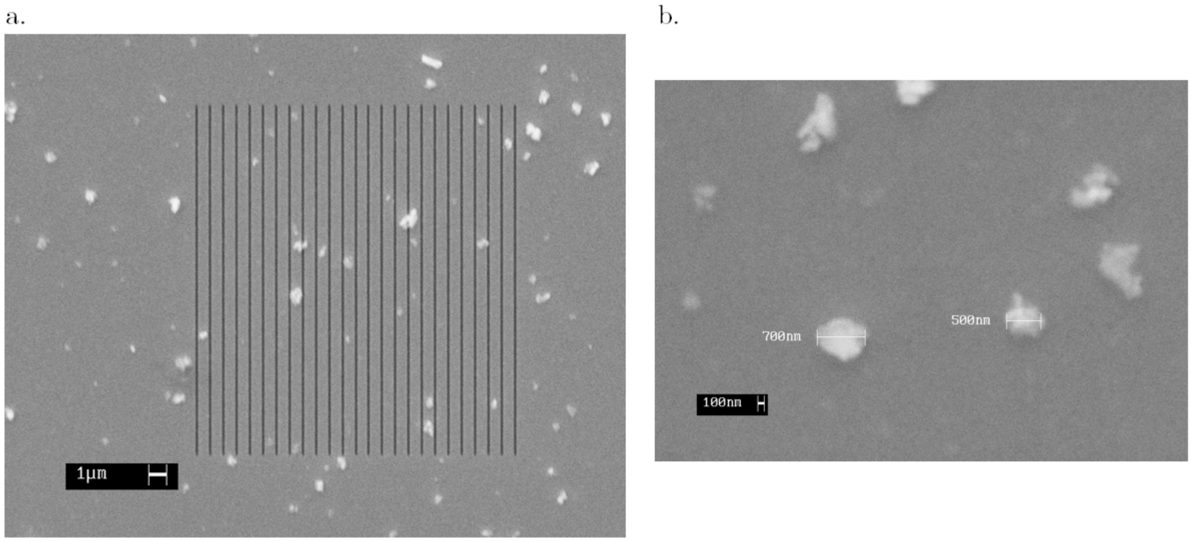

Figure 23 – a. SEM image of the nanostructure with thin film; b. SEM image details of the NPs showing the lateral size and shape.

Source: By the author.

Figure 24.a shows the AFM topology image of a nanostructure showing details of nanoslits and nanoparticles distribution immersed in PMMA film. Figure 24.b is the profile obtained from the indicated white dashed line indicated in 24.a. Using AFM, we determined that the thickness of the PMMA film is approximately 140 nm (confirmed using a contact profilometer), and in a flat gold surface region, the roughness measurement is about 0.155 nm (R_a) and the root mean square surface roughness of about 0.194 nm (R_q). The average NP density on the surface is 0.15 NP/μm^2 for the nanoglass methodology used in Chapter 3. It is important to note that the particular NP in Figure 24.b (the peak in Z around 4μm has a lateral diameter of approximately 300 nm and height, from the surface, of 250 nm; that is, about 50 nm of the NP is immersed in the PMMA film, which leads us to conclude that the NP is at 90 nm from the nanostructure (see Figure 24.c). In Figures 25.a and 25.b show the details of the nanostructure's AFM topography. In Figure 25.c, the profile of the nanoslits shows a depth of 11 nm and a width of 500 nm (without the PMMA film, the nanoslits have a depth of 100 nm and a width of 100 nm - see Figure 10). The small particles observed inside the slit can be due to the small glass NP or some other material left over during the process.

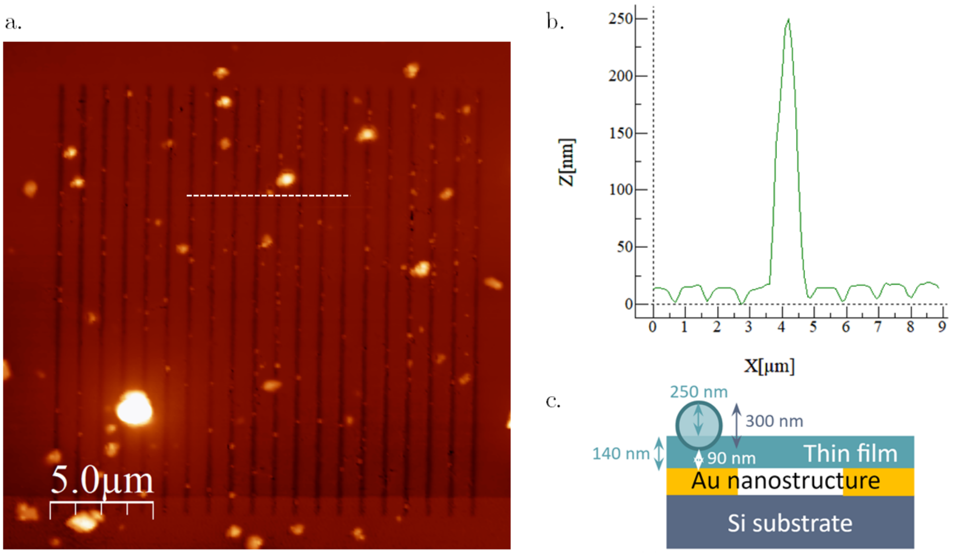

Figure 24 – a. AFM topography image of the nanostructure; b. Height profile on the indicated white dashed line in a.

Source: By the author.

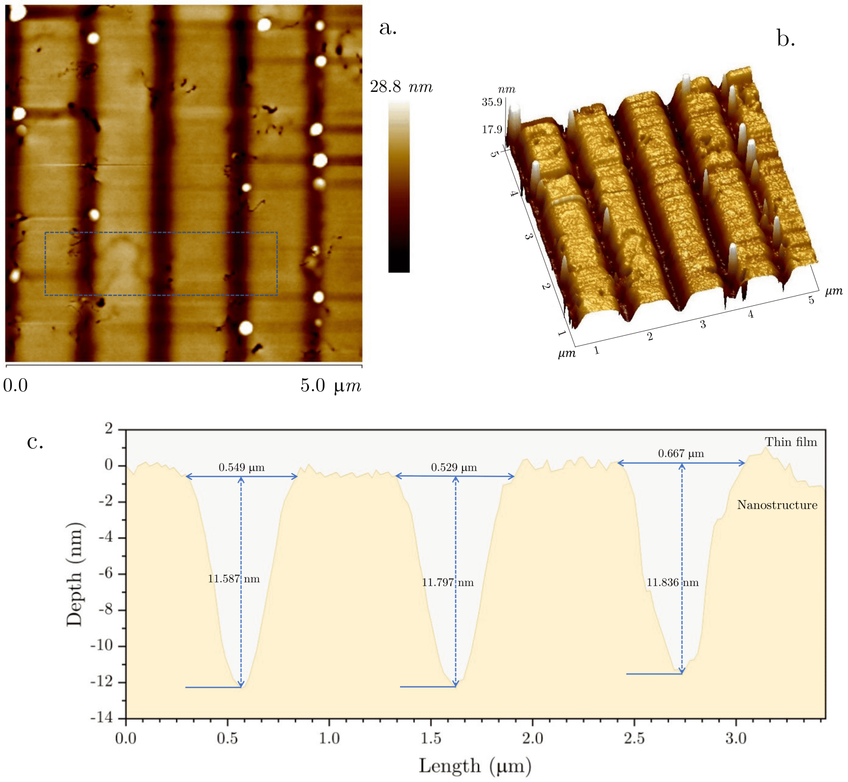

Figure 25 – a. AFM topography image of the nanostructure region; b. 3D image of the topography; c. Nanostructure line profile

Source: By the author.

5.2 Confocal imaging microscopy

The thin film's first confocal microscopy image was performed with a film deposited with the same methodology but on a crystalline silicon substrate. Crystalline Si does not show any visible luminescent process. Figure 26.a shows the hyperspectral image obtained by the confocal microscope. The spectral decomposition was taken in two different areas indicated as A and B in Figure 26.a The image clearly shows the green transition of the Er^{3+} located in the nanoglasses and that the PMMA film does not emit light.

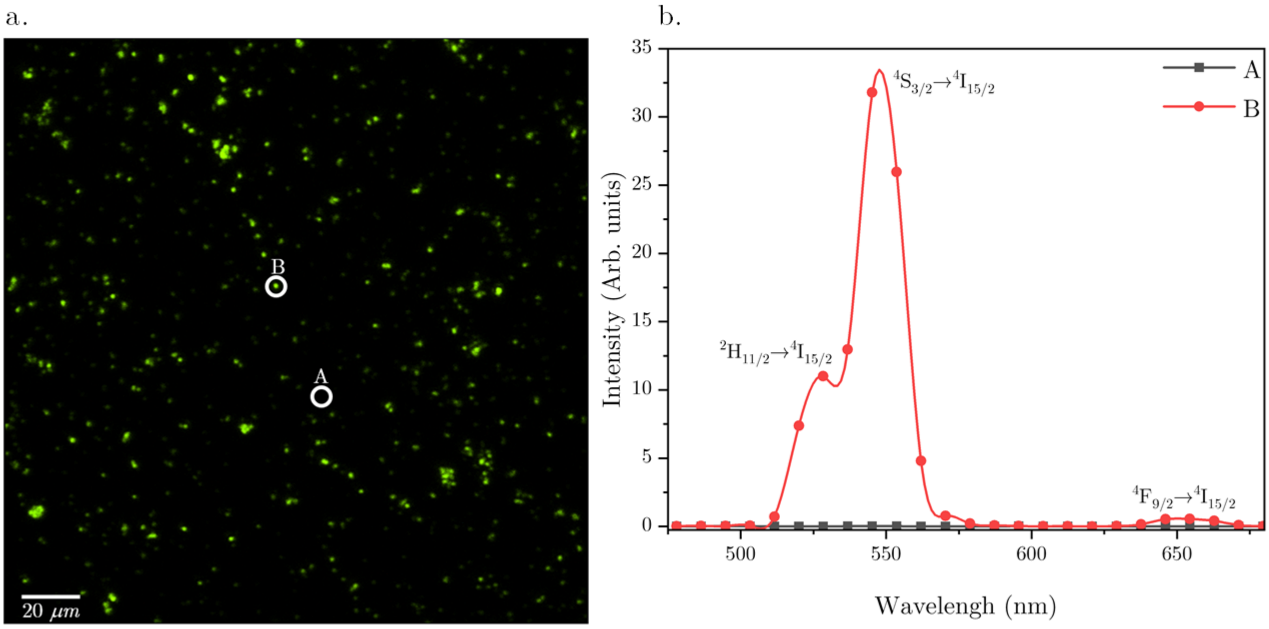

Figure 26 – a. Confocal microscope hyperspectral image excited with 1 mW/980 nm Ti:Saphire laser; b. Spectral decomposition of the areas indicated.

Source: By the author.

Figure 27 shows images of the same area of the thin film, which was obtained with three different excitation wavelengths. Spectral decomposition was performed in the same region indicated by the white circle whose spectra decompositions are shown in 27.d. The direct excitation at 405 nm has the lowest efficiency, showing the presence of the Er^{3+} green transition but with a background due to the emission of the gold film. For the excitations at 800 nm and 980 nm, individual nanoglasses with sizes below 0.5 μm can be distinguished. The hyperspectral images of the nanoglasses have similar behavior for distribution and homogeneity as the ones obtained by SEM and AFM in the previous section. The influence of SPPs generated by Au nanostructures on the emission of nanoglasses was carried out with laser excitations at 800 nm and 980 nm. The study was carried out in the same area with the same excitation potentials and kept the focus on the nanostructure and above.

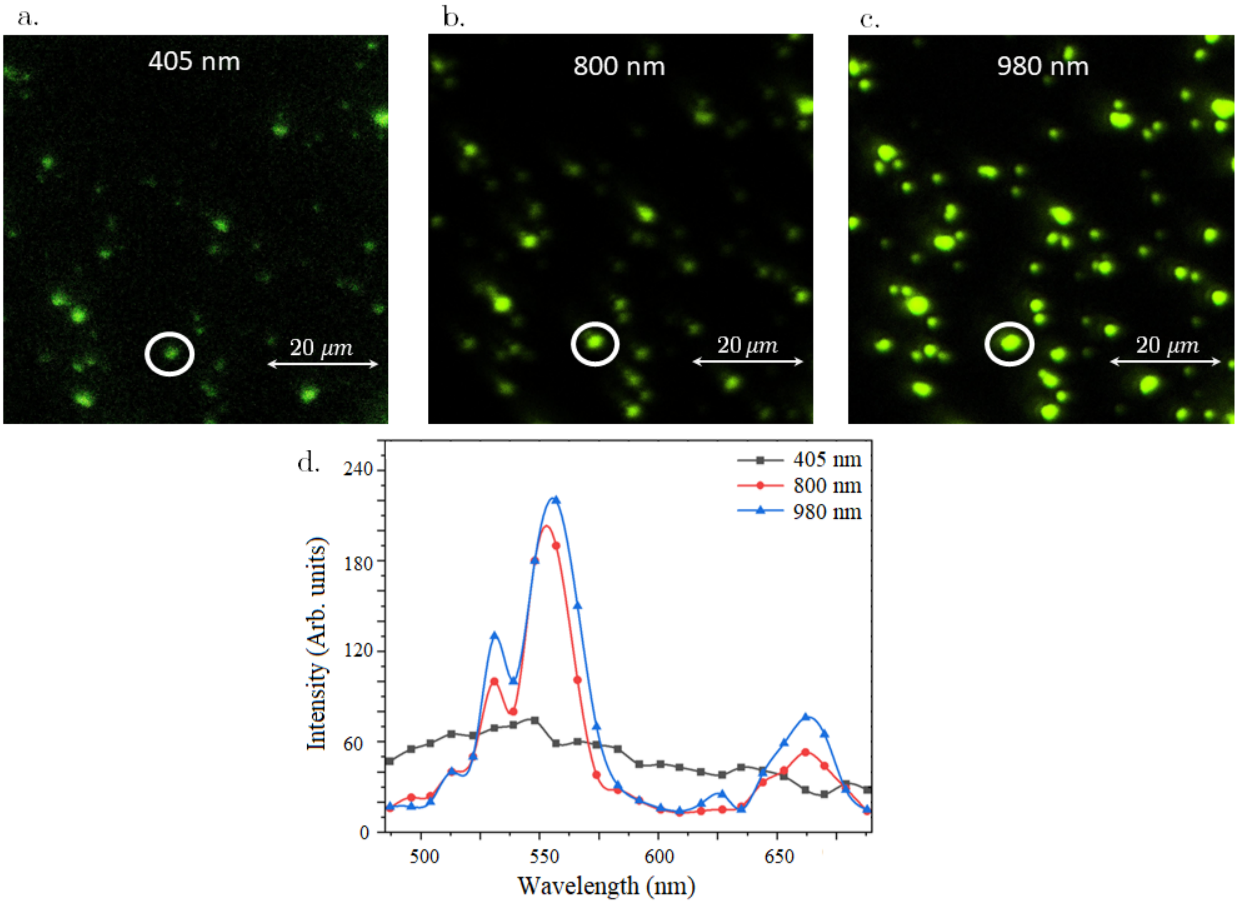

Figure 27 – Confocal microscope hyperspectral images of thin film excited with 3 different laser wavelengths; a. 10 mW/405 nm; b. 1 mW/800 nm; c. 1 mW/980 nm; d. Spectra of the area indicated in a., b. and c.

Source: By the author.

Figure 28 shows images of the same area of the Au nanostructures, which were obtained with two different excitation wavelengths. Direct excitation at 405 nm has the lowest efficiency, showing only Au emission. For the excitations at 800 nm, the region of the Au nanostructures and the presence of the SPPs generated in them can be distinguished. The study was carried out in the same area with the same excitation potentials and kept the focus on the nanostructure and above.

The results shown in Figures 27 and 28 indicate that the most efficient excitation wavelength to excite Er^{3+} ions is 980 nm and to generate SPP is 800 nm, respectively. The results for excitation at 800 nm and 980 nm are shown in Figure 29, Figure 30 and Figure 31.

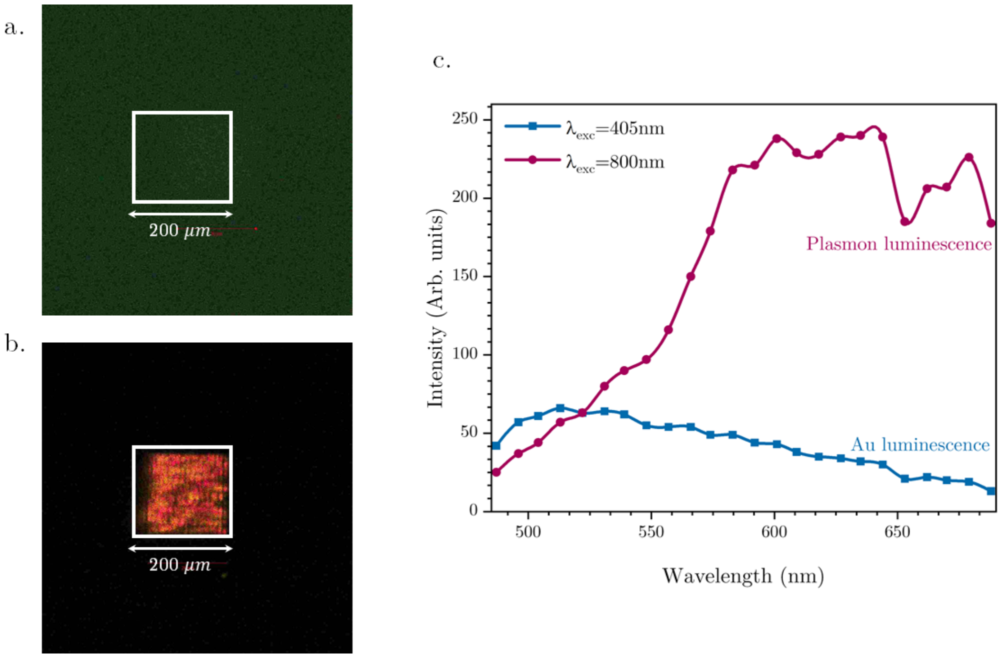

Figure 28 – Confocal microscope hyperspectral images of Au nanostructure excited with 2 different laser wavelengths; a. 1 mW/800 nm; b. 1 mW/980 nm and c. Spectra of the area indicated in a. and b.

Source: By the author.

The hyperspectral images analyses were measured in different areas (see Figure 29.a, 30.a and 31.a), such as outside (area A) and inside the nanostructure area (B, C, and D). Figures 29 correspond to laser excitation at 800 nm. Figures 30 and 31 correspond to laser excitation at 980 nm.

Figure 29.b shows the spectral decomposition of the areas A, B, C, and D. The area outside the nanostructure (A) shows a spectrum with well-defined Er^{3+} bands in the green and a small band in the red region. Area spectra on the nanostructure with and without nanoglasses (C and D, respectively) were compared. The spectrum of D corresponds to the long-band emission of Au nanoslits. On the other hand, in the C spectrum, a superposition was observed between the Er^{3+} bands in the green region and the long band corresponding to Au emission. The area of the nanoglasses on the nanostructure (B) shows a more intense spectrum than the other spectra. It was observed that the contribution of the Au background is also more intense, which is due to the intensity of the Er^{3+} bands in the green region also increasing, and this would indicate a plasmon-Er^{3+} coupling.

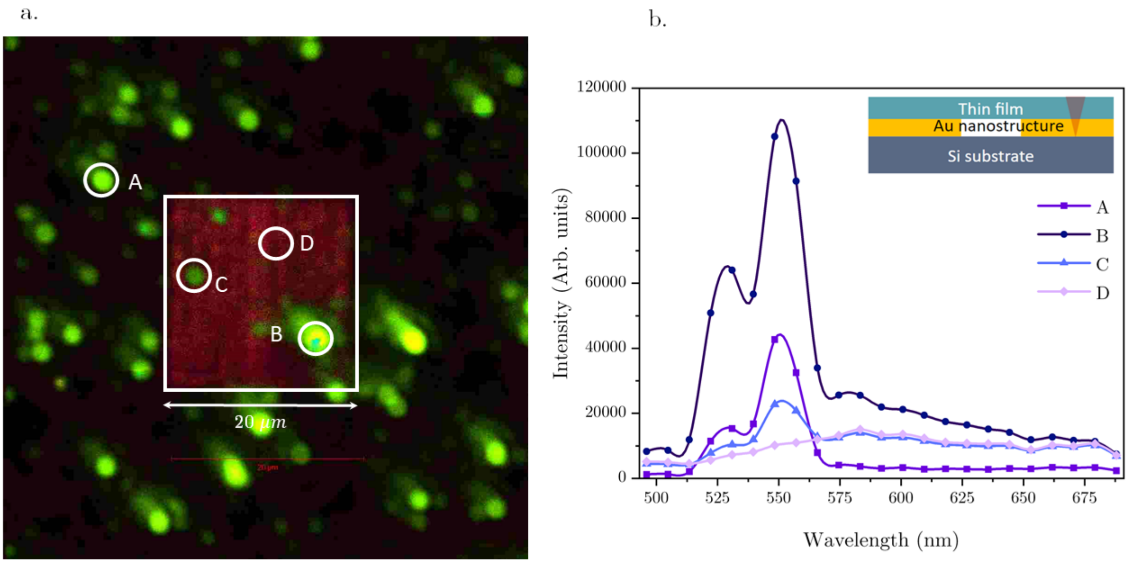

Figure 29 – a. Confocal microscope hyperspectral image excited with 1 mW/800 nm (in focus with the nanostructure); b. Spectral decomposition of the areas A, B, C, and D indicated.

Source: By the author.

Figures 30 and 31 correspond to laser excitation at 980 nm with the focal plane at the nanostructure and 0.2 μm above, respectively. It is interesting to note that the laser focusing on the nanostructure shows the same behavior for the spectra as those obtained with excitation at 800 nm. As for the image focused above the surface, it is possible to observe in all regions the clear presence of the green band of Er^{3+} (see Figure 31.b) and no longer the long band emission due to gold. Another interesting point is the behavior of the green band for regions A and B. Focusing on the nanostructure, the relative ratio between the intensities (B with respect to A) is greater, which is evidence of the SPPs coupling with the RE. The size of the nanoglass can also generate a similar effect.

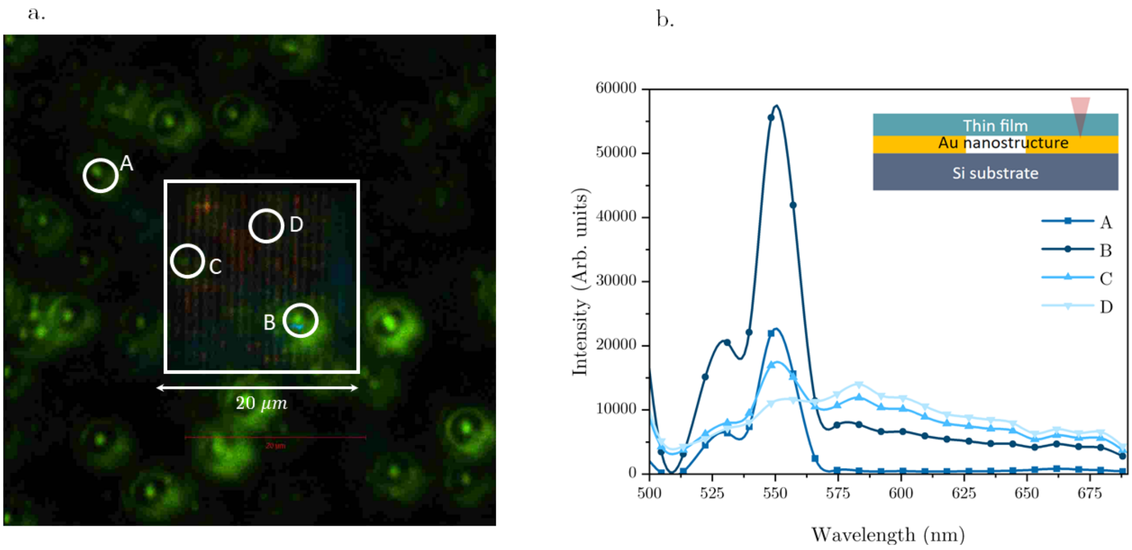

Figure 30 – a. Confocal microscope hyperspectral image excited with 1 mW/980 nm (in focus with the nanostructure); b. Spectral decomposition of the areas A, B, C, and D indicated in a.

Source: By the author.

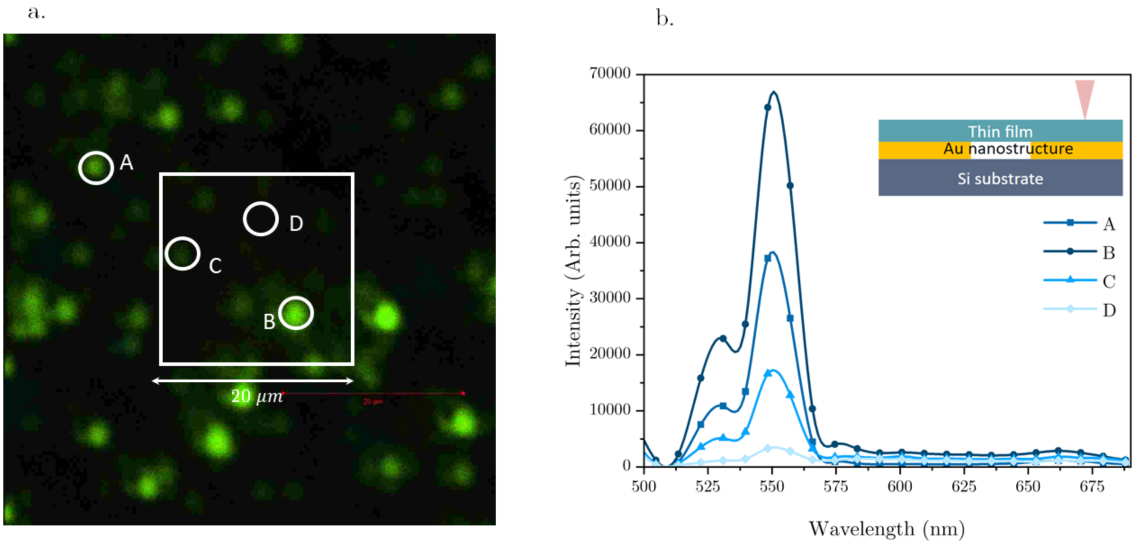

Figure 31 – a. Confocal microscope hyperspectral image excited with 1 mW/980 nm (above the focal plane of the nanostructure); b. Spectral decomposition of the areas A, B, C, and D indicated in a.

Source: By the author.

Considering that the Er^{3+} ions are inserted inside the nanoglasses and embedded in the PMMA, the coupling process is synthesized in the following steps:

1. When the incident light (800 nm or 980 nm) excites the system, part of it is absorbed by the nanoglasses that contain the Er^{3+} ions.
2. Due to the presence of the nanoslits, SPPs are generated at the metal-dielectric interface. These plasmons interact with the incident electromagnetic field.
3. The interaction between the plasmons generated in the nanoslits and the excited Er^{3+} ions of the nanoglasses allows energy transfer between them.

5.3 Fluorescence lifetime imaging

One of the main features of a confocal microscope is the ability to compose spectral images and combine the image measurement with electronic transition lifetimes, a technique known as Fluorescence Imaging Lifetime (FLIM). In this case, the acquisition can be made by filtering regions of interest in the spectrum. In the analysis, we used two detection channels labeled CH1 (500-540 nm) and CH2 (600-660 nm). FLIM analyses were performed in the same regions and under the same conditions as the results shown in Figures 29, 30, and 31.

The FLIM images in Figure 32.a was obtained in the same region and under the same conditions as Figure 29. The signal obtained in CH1 is much more intense than the CH2, as observed in 32.b. The decay curves have very peculiar characteristics: a fast decay of the order of 40 ps, a decay with a characteristic time between 220-300 ps, and in addition, a long decay that it is not possible to determine because it is outside the detection range (greater than 12 ns) and characterized by the background. The emission due to the nanoslits is evident in the nanostructure region. The fast decay is due to the system (laser and detection electronics – IRF), whereas the decay between the order of 250 ps comes from the energy exchange between the SPPs and RE. There may be an intermediate time below μs, which is the time for these transitions in the glass see Figure 21. In the FLIM 32.b (CH2) image, the behavior of nanoglasses inside and outside the nanostructure is evident (time contrast), which does not happen for CH1. Interestingly, in the spectral image (Figure 29, the contribution of the Er^{3+} emission's red band overlaps with the nanoslits' background.

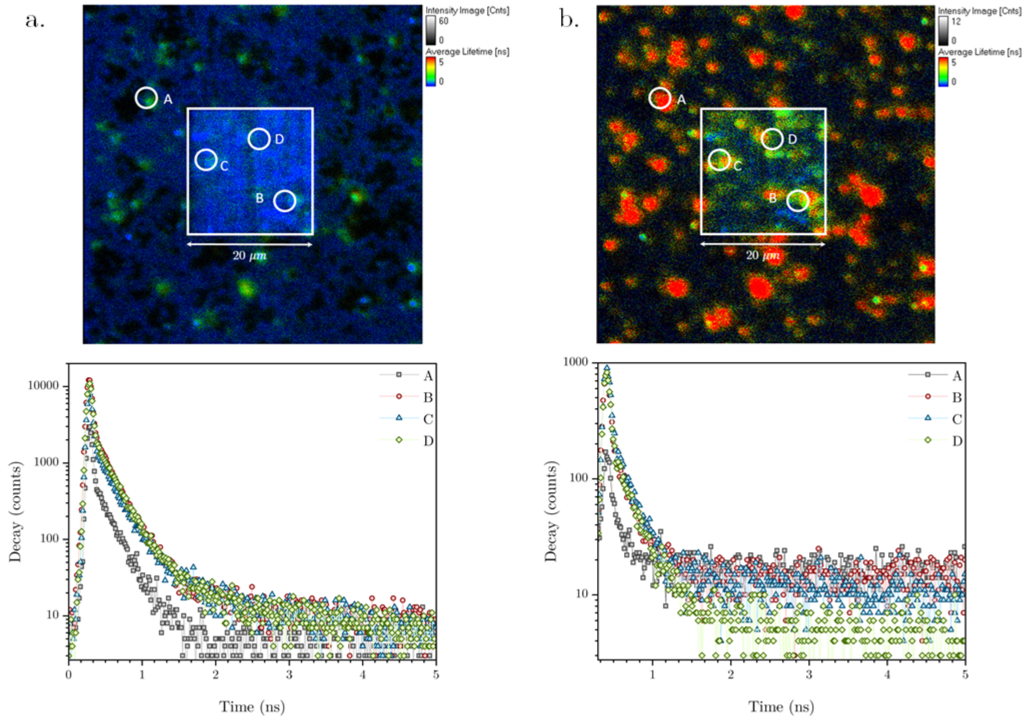

Figure 32 – FLIM images from the same region and conditions of Figure 29.a. CH1; b. CH2. The decay graphics below the images correspond to the time decomposition of the areas A, B, C, and D.

Source: By the author.

The Figures 33 and 34 were obtained in the same regions as the corresponding spectral images shown in Figures 30 and 31. The laser excitation laser was set to 980 nm in focus with the nanoslits and out of focus, respectively. Figure 34 shows the FLIM images, a fast decay time in CH1 appears as a background all over the image, more intense in the nanostructure region. This background may be due to the second harmonic generation on the gold surface and augmented by the generation of SPPs in the nanostructure region. In the FLIM images with the laser in focus were reported in Figure 33, the results show evidence of coupling in the green region, and in the red region, the long background is more pronounced.

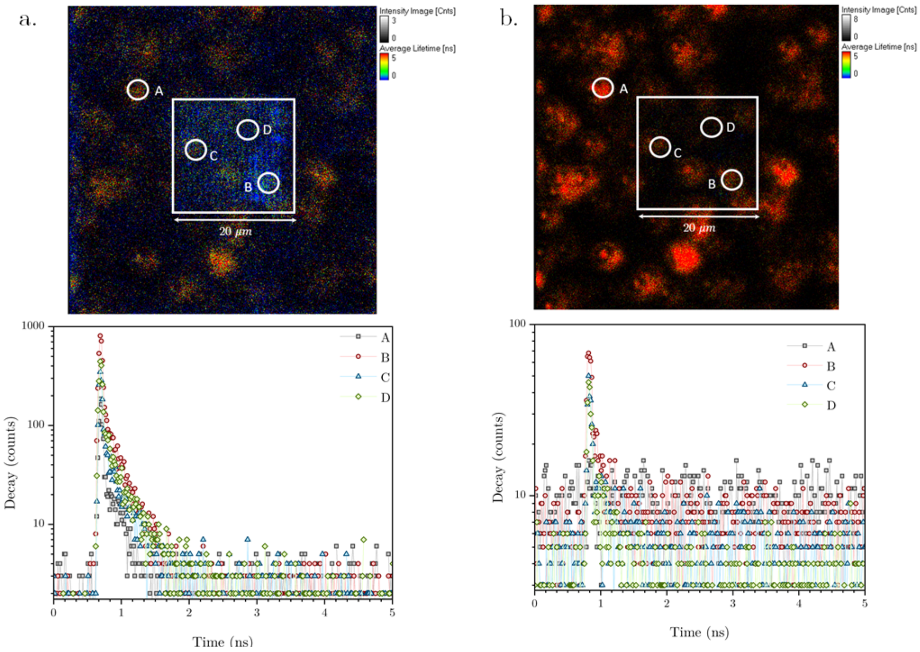

Figure 33 – FLIM images from the same region and conditions of Figure 30 in focus with the nanostructure. a. CH1; b. CH2; The decay graphics below the images correspond to the time decomposition of the areas A, B, C, and D.

Source: By the author.

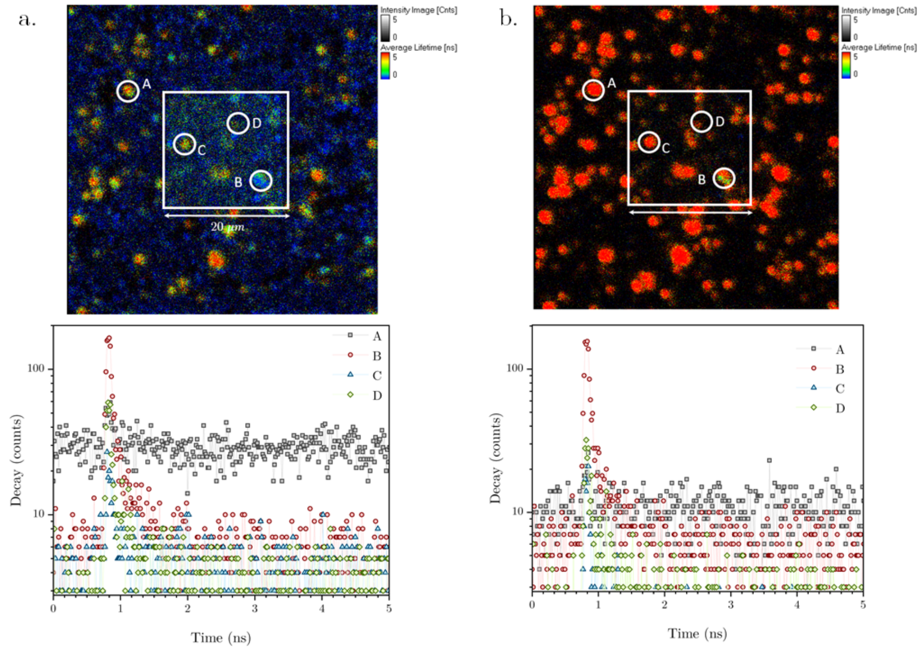

Figure 34 – FLIM images from the same region and conditions of Figure 31 above the nanostructure. a. CH1; b. CH2; The decay graphics below the images correspond to the time decomposition of the areas A, B, C, and D.

Source: By the author.

The previous results show that the SPPs and RE coupling is much more evident with laser excitation at 800 nm and for the Er^{3+} red band region (CH2). To verify our hypothesis, we performed an analysis with another nanostructure (the same parameters as those used in the previous analyses) with a different distribution of nanoglasses. The results of this analysis are presented in Figure 35 clearly show that for the red emission of Er^{3+} (CH2) the SPPs and RE interaction modify the lifetime of the emission.

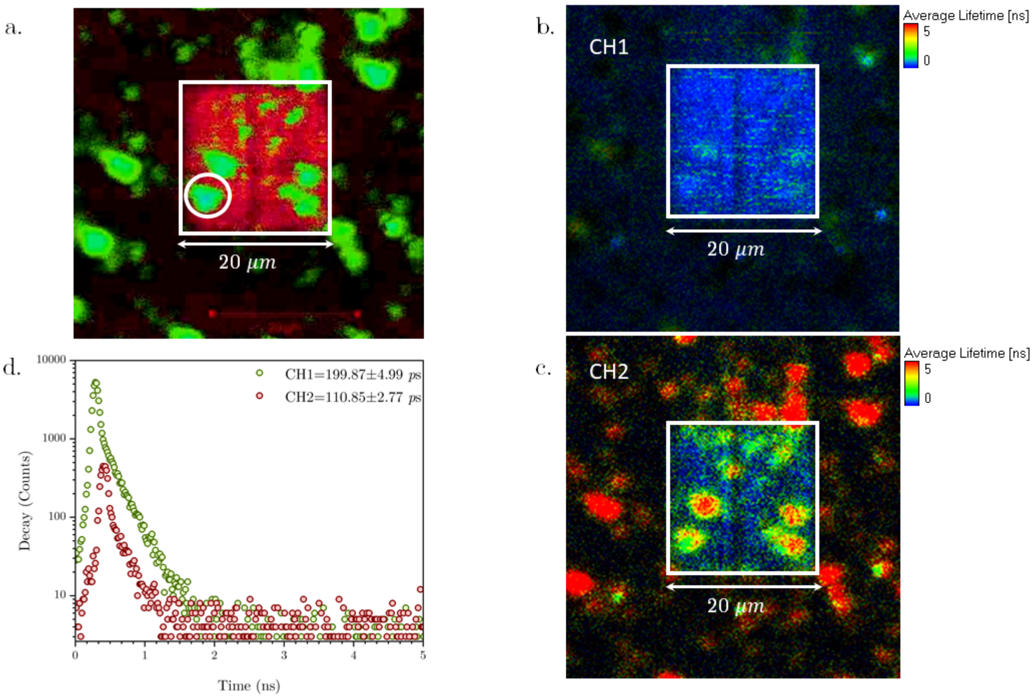

Figure 35 – a. Spectral and FLIM images; a. Spectral image with laser 1 mW/800 nm in focus with the surface; b. FLIM image CH1; c. FLIM image CH2; d. The decay decomposition of the white circle indicated in a.

Source: By the author.

In Appendix C, the results of fluorescence lifetime imaging (FLIM) are presented for a germanate-tellurite glass sample doped with 0.1 mol% Er_2O_3 and was conducted in CH1 and CH2 channels under 980 nm excitation. The typical time scale for FLIM measurements in the confocal microscope is in the ns range. In contrast, the intrinsic radiative lifetime of Er^{3+} ions in that spectral region are μs. Longer lifetimes appear as a long background.

5.4 Microluminescence in the infrared region

The $^4I_{13/2}$ transitions (1530 nm) to $^4I_{15/2}$ of Er^{3+} ion are particularly important due to their use in telecommunication. Figure 20 shows the results of the characterizations for the glasses. Spectral imaging measurements in the near-infrared region with resolutions like those obtained in the previous section are particularly difficult to perform. To study these transitions in thin films, we used the Micos-Horiba microluminescence system, in which it is possible to map the region on the nanostructure with 3-4 μm resolution. Figure 36 shows a composite made with a map of 36.a and 36.b region. In all measurements carried out on different nanostructures, not just this one in particular, we verified an increase in emission (see 36.c). The density of the nanoglasses can also affect the intensity of the signal as the resolution is not in the order of the nanoparticle size. As the infrared transitions have a longer lifetime, the decrease can also be measured in the strength of the coupling.

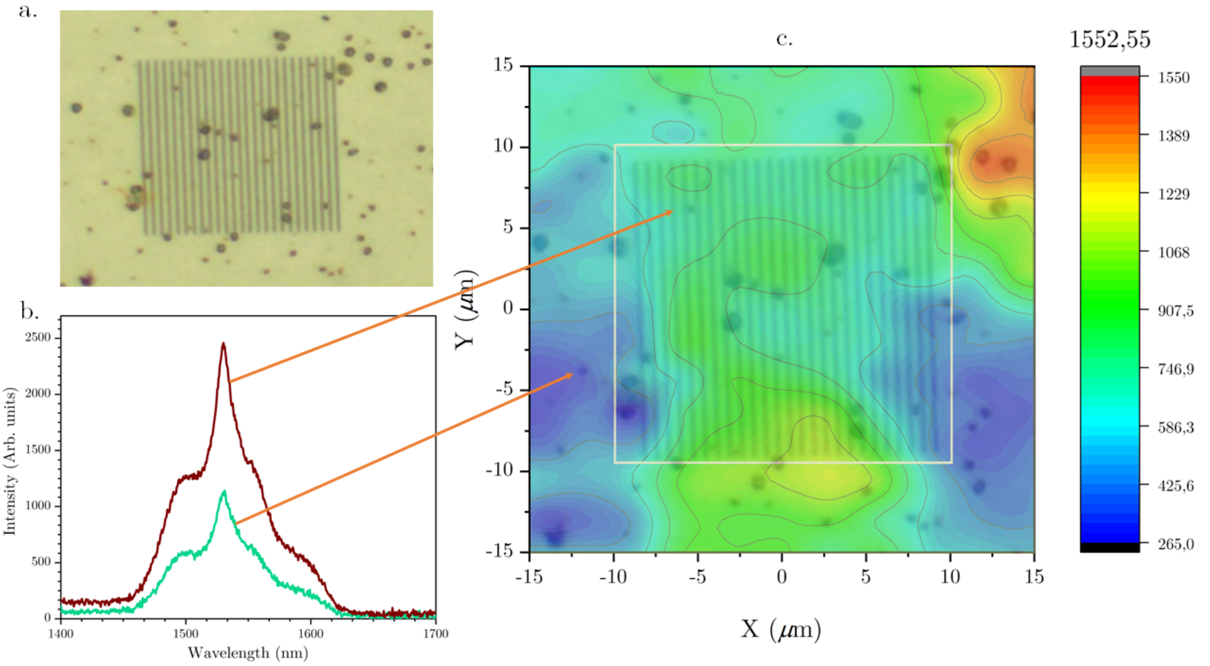

Figure 36 – a. Optical image of the nanostructure region, b. PL of nanostructure region indicated with arrows, c. Intensity map of the 1552 nm wavelength composed with the optical image in the background

Source: By the author.

5.5 Transfer energy mechanisms

The mechanism to explain the increase of luminescence and reduction of the radiative lifetime of Er^{3+} via plasmonic nanostructures is present in Figure 37. The process begins when the system is excited with two 980 nm photons (Uc process). The electron is excited to the $^4F_{7/2}$ state. When the electron is in this state, it decays non-radiatively to the $^2H_{11/2}$ state and instead of decaying radiatively towards the $^4I_{5/2}$ state (a process of the order of μs), it transfers energy to state $|1\rangle$ of the SPP, due to coupling plasmon-Er^{3+}. Then, the electron decays radiatively from state $|1\rangle$ to state $|0\rangle$ (a process on the order of ps).

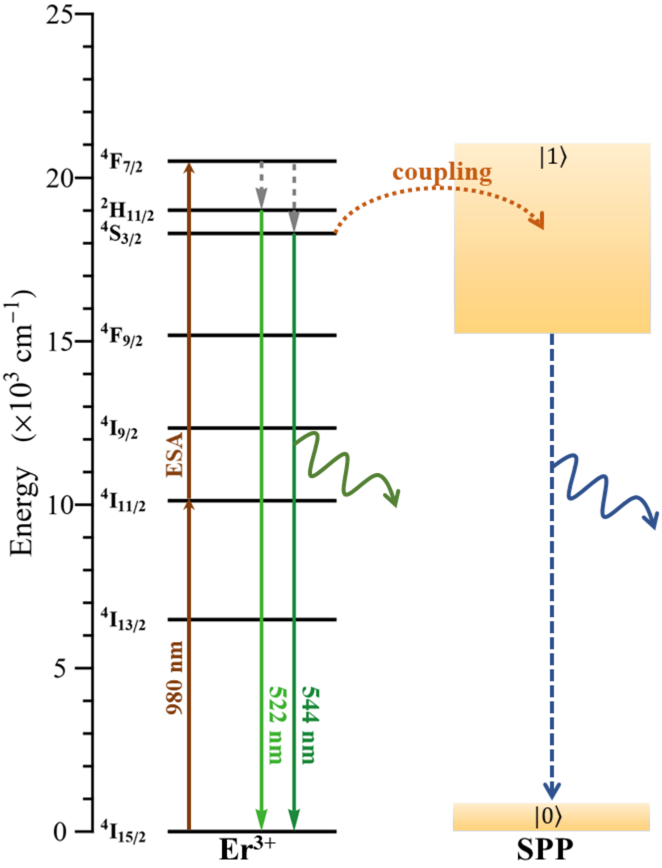

Figure 37 – Plasmon-Er^{3+} coupling diagram under excitation of 980 nm.

Source: By the author.

Figure 38 shows that when excited with two 800 nm photons (Uc process). The electron is excited to a state close to the conduction band. When the electron is in this state, it can decay non-radiatively to the $^4F_{7/2}$ state and follow the mechanism presented in Figure 37, or directly decay to the $|1\rangle$ state of the SPP, because with 800 nm excitation the generation of SPP is more efficient. Then, the electron decays radiatively from state $|1\rangle$ to state $|0\rangle$ (a process on the order of ps).

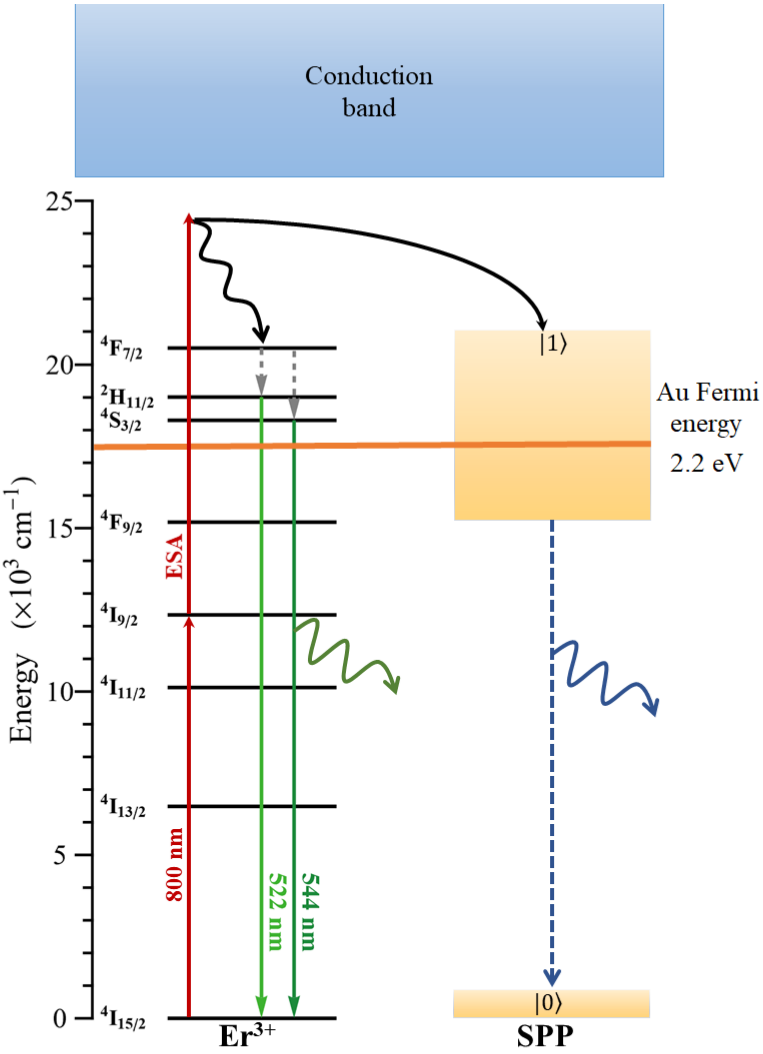

Figure 38 – Plasmon-Er^{3+} coupling diagram under excitation of 800 nm.

Source: By the author.

Plasmon-Er^{3+} coupling ions can increase the radiative emission rate of Er^{3+} ions, resulting in more intense light emission. This improvement in light emission is due to the strong coupling and local field modification provided by the plasmons, which increases the radiation efficiency of the system.

The coupling occurs when the natural frequency of the plasmon (ω_p) is close to the Er^{3+} emission frequency. This is why the measured emissions have the same spectral shape as the Er^{3+} emission and are highly polarized with the SPPs formed at the metal-dielectric interface. This type of coupling generates a photon-plasmon effect, where light travels across the metal-dielectric interface as a plasmon and leaves the system to be detected as photons.

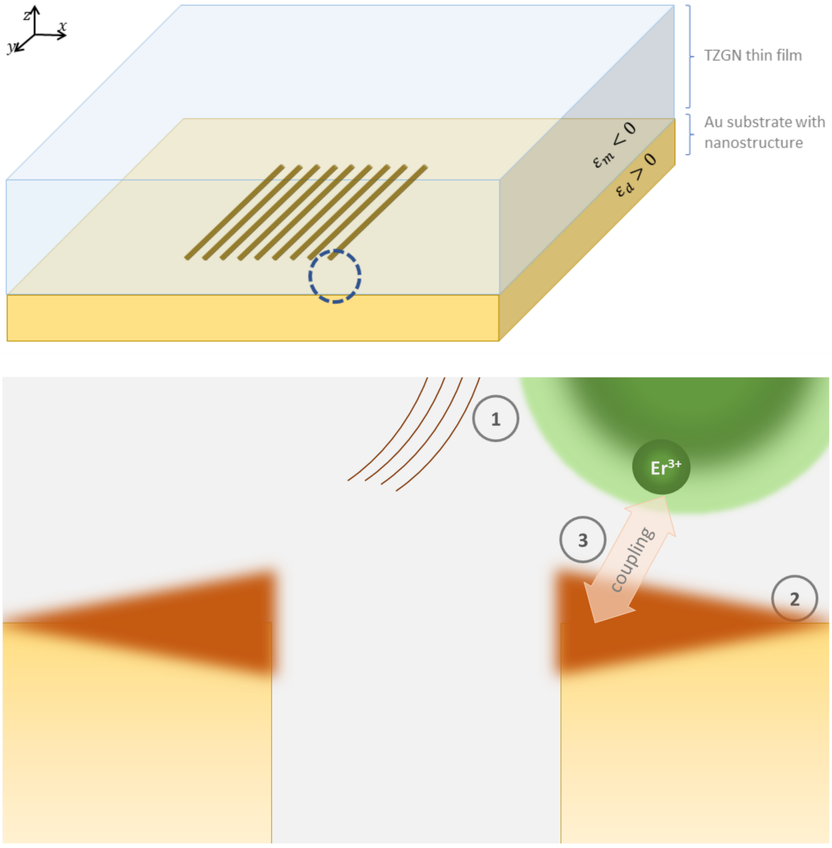

Figure 39 – Plasmon-Er^{3+} coupling.

Source: By the author.

Figure 39 shows that when an Er^{3+} ion is close to an Au nanoslit, this leads to a strong interaction between them. So, when the Er^{3+} ion emits light, this emission couples with the SPPs. This would improve the local field around the nanoslit, significantly increasing the radiative emission rate of Er^{3+}, which produces a shortening of the radiative lifetime of Er^{3+}. To simplify, the Er^{3+} ion was considered as a two-level quantum emitter (Qe), which is located near the metal-dielectric interface and the frequency of the transition of the excited state $|1\rangle$ to the ground state $|0\rangle$ is γ_{Qe} and its emission probability is q. The quantum emitter excitation process is via SPP, and the emission rate was described as:

$$\gamma_{em} = q\gamma_{exc} \tag{5.1}$$

where γ_{em} and γ_{exc} are the emission and excitation rate, respectively. In the case of the electric dipole it is proportional to $|\mathbf{p} \cdot \mathbf{E}|^2$, where $\mathbf{E}$ is the local excitation field. Then, the transition probability is expressed using Fermi's golden rule:

$$\gamma_{em} = \frac{2\omega_{Qe}}{3\hbar\epsilon_d}|p_{Qe}|^2 g(r, \omega_{Qe}) \tag{5.2}$$

where g represents the density of states of the system, which is strongly modified by the presence of SPP, causing a reduction in the lifetime of Qe.

6 CONCLUSIONS AND PERSPECTIVES

6.1 Conclusions

In this dissertation, the results obtained in the study of germano-tellurite glasses and thin films were presented, and a coupling mechanism between Plasmon and Er^{3+} ion was proposed.

The first part presented the spectroscopic properties of the studied glasses and the impact of Er^{3+} ion doping on their physical properties. The XRD patterns showed the absence of three-dimensional periodicity of the crystal lattice in the glass samples, confirming their amorphous behavior. Through FTIR, the transmission of glasses in the infrared region was analyzed. Absorption bands corresponding to functional groups present on the glass surface were observed. Measurements of the refractive index of the glasses were made and adjusted to the Sellmeir equation. High refractive index values were obtained, indicating the high density of the glass and the lack of significant changes with Er^{3+} concentration. Absorption measurements were carried out in the UV-VIS-NIR region, where absorption bands corresponding to electronic transitions of Er^{3+} ions were observed. Direct and indirect energy gaps were calculated using the Tauc-Meth model. An increase in the Urbach energy was observed with increasing Er^{3+} concentration, indicated by an increase in the structural disorder of the glasses. Then Raman spectroscopy revealed changes in the energy of the phonons. The influence of increased Er^{3+} doping on NBO generation was reported, indicating a modification in the glassy matrix due to the presence of Er^{3+} ions.

Furthermore, the Uc spectra revealed the presence of three distinct emission bands attributed to Er^{3+} ions when excited at 980 nm. These bands correspond to the transitions: $^2H_{11/2} \rightarrow ^4I_{15/2}$, $^4S_{3/2} \rightarrow ^4I_{15/2}$ and $^4F_{9/2} \rightarrow ^4I_{15/2}$, centered at 520 nm, 550 nm, and 660 nm, respectively. Among all samples, the emission in the green region (520 nm and 550 nm) was found to be predominant. Interestingly, in the TZGN100 glasses, a variation in the intensities of the peaks constituting the 530 nm band was observed, which could be attributed to alterations in the ion-ion energy transfer process or fluorescence quenching. Conversely, the emission in the red region (660 nm) exhibited significantly lower intensity than the green emission, consistently observed across all samples. These findings suggest that the crystalline field created by the germano-tellurite glass matrix favors green emission over red emission from Er^{3+} ions. Additionally, excitation at 980 nm resulted in emission in the NIR region centered at 1530 nm. Furthermore, an increase in FWHM was observed, indicating a broader bandwidth associated with the higher concentration of Er^{3+} ions. These outcomes highlight the potential of TZGN glasses as promising candidates for infrared (IR) amplifiers, leveraging their emission in the near NIR region. Finally, radiative lifetime measurements were conducted for the $^2H_{11/2}$ (526 nm), $^4S_{3/2}$ (546 nm) and $^4I_{13/2}$ (1530 nm) transitions. Variations in the radiative lifetimes were observed, depending on the spectral region and the concentration of Er^{3+} ions. These observations provide valuable insights into the impact of Er^{3+} doping on germanate-tellurite glasses' structural and optical characteristics. Furthermore, these findings hold significance for optimizing manufacturing processes and exploring potential technological applications of these materials.

The second part presented the thin films fabricated by means of the spin-coating technique of the nanoglasses and PMMA. The morphology of the thin films was studied through SEM and AFM measurements, and the average size of the nanoparticles incorporated within the PMMA matrix was approximately 300nm. Two samples were obtained: one was deposited on a pure Si substrate, and the other was deposited on an Au substrate containing an array of nanoslits (metasurface). The AFM topographic images of the thin films deposited on the pure Si substrate revealed homogeneous surfaces with an R_a of approximately 0.155 nm and an R_q of approximately 0.194 nm. By comparing the height differences between areas with and without the film, the film thickness was estimated to be around 140 nm. For the thin films deposited on the Au substrate with nanoslits, the roughness measurements in the region above the slits showed an R_a of 4.11 nm and an R_q of 4.72 nm. Additionally, the penetration depths of the thin film over the slits were approximately 11 nm. These findings provide valuable insights into the surface morphology and characteristics of thin films. The results contribute to our understanding of the fabrication and properties of these films, which may have implications for various technological applications.

Through confocal microscope imaging, spectral and FLIM images analysis, we confirmed that PMMA does not luminesce under 800 nm and 980 nm excitation. Thus, it does not interfere with the emission bands of Er^{3+} ions. The 405 nm laser excitation is not efficient in carrying out the measurements. Measurements on the nanostructured thin films deposited on nanoslits led to the generation of SPP at the Au-PMMA interface. These plasmons interact with the incident electromagnetic field. The FLIM images clearly show the change in the lifetime emission in the area of the metasurface and suggest a plasmon-Er^{3+} coupling. This coupling can also enhance the radiative emission rate of Er^{3+} ions, resulting in more intense light emission, but the size of the glass nanoparticle can also act in the same direction. The decrease in the lifetimes from the order of μs to ps is the signature of the plasmon-Er^{3+} coupling. These conclusions provide valuable insights into the plasmon-Er^{3+} coupling phenomenon and its impact on light emission. This understanding is crucial for developing new optical devices and applications that utilize these coupling effects.

6.2 Perspectives

In order to improve the glass nanostructuring process, other equipment could be used. In this master's dissertation, a rotational mill was used for 200 hours at 35 rpm. There is other equipment on the market, such as high-energy vibration mills, which could reduce the grinding time and also the grain size, the use of this type of mills would be an alternative for future work. In addition, carrying out a study of the relationship between grinding time and grain size would provide additional information to optimize these nanostructuring processes.

In order to disaggregate and optimize the distribution of nanoglasses in thin films, high-power ultrasound equipment could be used. Alternate thin film deposition methods could also be tried. Pulsed laser deposition using bulk glass as a target would be an option to obtain thinner films and better distribution.

For future work in the area of quantum-plasmon interaction research, the study could be opened to other quantum emitters. Apart from doping glasses with Er3+ ions, we could study the coupling with other rare earth ions such as Pr^{3+}, Yb^{3+}, Tm^{3+}, Nd^{3+}. Furthermore, taking into account that glasses are excellent host materials for doping with quantum emitters, they could also be doped with perovskite oxides that have ABX_3 structures, where A and B are cations and X is an anion, or with colloidal quantum dots of cadmium sulfates (CdS), cadmium selenites (CdSe) or indium arsenites (InAs). Thus we would open a range of interactions between quantum emitters and surface polariton plasmons.

REFERENCES

1 BERINI, P.; LEON, I. D. Surface plasmon–polariton amplifiers and lasers. **Nature Photonics**, v. 6, p. 16–24, 2012. ISSN 1749-4885.

2 MAIER, S. A. **Plasmonics**. Berlin: Springer, 2007. ISBN 978-0-387-33150-8.

3 ÇAMIçI, H. C. *et al.* The role of tungsten oxide in Er3+-doped bismuth-germanate glasses for optical amplification in L-band. **Scientific Reports**, v. 13, p. 8835, 2023. ISSN 2045-2322.

4 PULLAIAH, G. *et al.* Green emission characteristics of Er3+ -doped TeO2-WO3-GeO2 glasses through up and down conversion processes. **Journal of Non-Crystalline Solids**, v. 615, p. 122413, 2023. ISSN 00223093.

5 YU, H. *et al.* Plasmon-enhanced light–matter interactions and applications. **npj Computational Materials**, v. 5, p. 45, 2019. ISSN 2057-3960.

6 GüSKEN, N. A. *et al.* Emission enhancement of erbium in a reverse nanofocusing waveguide. **Nature Communications**, v. 14, p. 2719, 2023. ISSN 2041-1723.

7 YANG, J. *et al.* Manipulation of the dephasing time by strong coupling between localized and propagating surface plasmon modes. **Nature Communications**, v. 9, p. 4858, 2018. ISSN 2041-1723.

8 MORSE, D. L.; EVENSON, J. W. Welcome to the glass age. **International Journal of Applied Glass Science**, John Wiley and Sons, Ltd, v. 7, n. 4, p. 409–412, 2016. ISSN 2041-1294.

9 YAMANE, M.; ASAHARA, Y. **Glasses for photonics**. London: Cambridge University Press, 2000.

10 MAURO, J. C.; ZANOTTO, E. D. Two centuries of glass research: historical trends, current status, and grand challenges for the future. **International Journal of Applied Glass Science**, John Wiley and Sons, Ltd, v. 5, n. 3, p. 313–327, 2014. ISSN 2041-1294.

11 JENNISKENS, P.; BLAKE, D. F. Structural transitions in amorphous water ice and astrophysical implications. **Science**, American Association for the Advancement of Science, v. 265, n. 5173, p. 753–756, 1994. ISSN 00368075.

12 MARI, E. A. **Los vidrios**. Madrid: Editorial Américalee, 1982.

13 ZARZYCKI, J. **Les verres et l'état vitreux**. Paris: Elsevier, 1982.

14 SHELBY, J. **Introduction to glass science and technology**. London: Royal Society of Chemistry, 1997.

15 RAO, K. J. **Structural chemistry of glasses**. Amsterdam: Elsevier, 2002.

16 VARSHNEYA, A. K.; MAURO, J. C. Comment on misconceived astm definition of "glass" by A. C. Wright. **European Journal of Glass Science and Technology Part A**, v. 51, p. 28–30, 2010. ISSN 00171050.

17 ZANOTTO, E. D.; MAURO, J. C. The glassy state of matter: its definition and ultimate fate. **Journal of Non-Crystalline Solids**, Elsevier B.V., v. 471, p. 490–495, 2017. ISSN 00223093.

18 MAURO, J. C. *et al.* Nonequilibrium viscosity of glass. **Physical Review B**, American Physical Society, v. 80, n. 9, p. 094204, 2009. ISSN 10980121.

19 EL-DAMRAWI, G. *et al.* Characterization of new categories of bioactive based tellurite and silicate glasses. **Silicon**, Springer, v. 9, p. 503–509, 2014. ISSN 1876-9918.

20 THAMMA, U. *et al.* Nanostructure of bioactive glass affects bone cell attachment via protein restructuring upon adsorption. **Scientific Reports**, Nature Publishing Group, v. 11, p. 1–14, 2021. ISSN 2045-2322.

21 ARAUJO, C. B. de *et al.* Optical properties of glasses and glass-ceramics for optical amplifiers, photovoltaic devices, color displays, optical limiters, and random lasers. **Optical Materials**, North-Holland, v. 131, p. 112648, 2022. ISSN 0925-3467.

22 OULMAATI, L. *et al.* Comparison of energy transfer between terbium and ytterbium ions in glass and glass ceramic: Application in photovoltaic. **Solar Energy Advances**, Elsevier, v. 2, p. 100012, 2022. ISSN 2667-1131.

23 LOZANO, G. *et al.* Cold white light emission in tellurite-zinc glasses doped with Er3+–Yb3+–Tm3+ under 980 nm. **Journal of Luminescence**, North-Holland, v. 228, p. 117538, 2020. ISSN 0022-2313.

24 SANTOS, S. N. *et al.* Waveguides fabrication by femtosecond laser in Tb3+/Yb3+ doped CaLiBO glasses. **Optics and Laser Technology**, Elsevier, v. 140, p. 107030, 2021. ISSN 0030-3992.

25 EL-MALLAWANY, R. **Tellurite glass smart materials**. Amsterdam: Springer, 2018.

26 RIVERA, V.; MANZANI, D. **Technological advances in tellurite glasses**. Berlin: Springer, 2017. v. 254. ISBN 978-3-319-53036-9.

27 JHA, A. *et al.* Rare-earth ion doped TeO2 and GeO2 glasses as laser materials. **Progress in Materials Science**, Pergamon, v. 57, p. 1426–1491, 2012. ISSN 0079-6425.

28 GRELOWSKA, I. *et al.* Structural and optical study of tellurite–barium glasses. **Journal of Molecular Structure**, v. 1126, p. 219–225, 2016. ISSN 00222860.

29 YADAV, A. K.; SINGH, P. A review of the structures of oxide glasses by raman spectroscopy. **RSC Advances**, The Royal Society of Chemistry, v. 5, p. 67583–67609, 2015. ISSN 2046-2069.

30 CLABEL, J. L. *et al.* **Overall aspects of glasses for photonic devices**. Amsterdam: Elsevier, 2023.

31 MANNING, S. *et al.* Ternary tellurite glasses for the fabrication of nonlinear optical fibres. **Optical Materials Express**, v. 2, p. 140, 2012. ISSN 2159-3930.

32 JHA, A. *et al.* Review on structural, thermal, optical and spectroscopic properties of tellurium oxide based glasses for fibre optic and waveguide applications. **International Materials Reviews**, v. 57, p. 357–382, 2012. ISSN 0950-6608.

33 REDDY, B. N. K. *et al.* Study of RE ion-doped oxide glass materials for photonic applications. **Spectroscopy of Lanthanide Doped Oxide Materials**, Elsevier Inc., p. 293–304, 2019.

34 RIVERA, V. A. G. *et al.* **Collective plasmon-modes in gain media**. Berlin: Springer, 2015.

35 HOSSAIN, M. K. *et al.* Current applications and future potential of rare earth oxides in sustainable nuclear, radiation, and energy devices: A review. **ACS Applied Electronic Materials**, v. 4, p. 3327–3353, 2022. ISSN 2637-6113.

36 QIU, J. *et al.* Recent progress on upconversion luminescence enhancement in rare-earth doped transparent glass-ceramics. **Journal of Rare Earths**, v. 34, p. 341–367, 2016. ISSN 10020721.

37 SUN, L.-D. *et al.* Upconversion of rare earth nanomaterials. **Annual Review of Physical Chemistry**, v. 66, p. 619–642, 2015. ISSN 0066-426X.

38 SINGH, R. *et al.* Emerging applications of upconverting nanoparticles in intestinal infection and colorectal cancer. **International Journal of Nanomedicine**, Dove Medical Press Ltd., v. 14, p. 1027–1038, 2019. ISSN 11782013.

39 AUZEL, F. History of upconversion discovery and its evolution. **Journal of Luminescence**, v. 223, p. 116900, 2020. ISSN 00222313.

40 TAHERUNNISA, S. *et al.* Effect of up-conversion luminescence in Er3+ doped phosphate glasses for developing erbium-doped fibre amplifiers and g-led's. **Optical Materials: X**, Elsevier, v. 3, p. 100034, 2019. ISSN 2590-1478.

41 SUN, J. *et al.* Fabrication of pi phase-shifted fiber bragg grating and its application in narrow linewidth 1.5 um Er-doped fiber lasers. **Optics Communications**, v. 407, p. 344–348, 2018. ISSN 00304018.

42 LIU, Y. *et al.* Broadband luminescence at 1.5 um of Er Pr co-doped high silica glass by nanoporous doping technology. **Journal of Non-Crystalline Solids**, v. 575, p. 121206, 2022. ISSN 00223093.

43 HASSAN, S. M.; KITAMOTO, Y. Synthesis and characterization of sub-micrometer SiO2@NaYF4:Yb/Er beads and NaYF4:Yb/Er capsules for biomedical applications. **Electrochimica Acta**, v. 183, p. 160–164, 2015. ISSN 00134686.

44 GU, M. *et al.* Recent progress of rare earth doped hydroxyapatite nanoparticles: Luminescence properties, synthesis and biomedical applications. **Acta Biomaterialia**, v. 148, p. 22–43, 2022. ISSN 17427061.

45 BALARAMA, S. *et al.* Synthesis of Er2O3 blended CeO2 nanocomposites and investigation of their biomedical applications. **Chemical Physics Impact**, p. 100167, 2023. ISSN 26670224.

46 ALBALAWI, F. S. Efficacy of Er, Cr: YSGG laser phosphoric acid gel and riboflavin activated by photodynamic therapy on enamel reconditioning rebonded to metallic brackets: An invitro study. **Photodiagnosis and Photodynamic Therapy**, v. 40, p. 103043, 2022. ISSN 15721000.

47 KOSTKA, P. *et al.* Luminescence, up-conversion and temperature sensing in Er-doped TeO2-PbCl2-WO3 glasses. **Journal of Non-Crystalline Solids**, v. 553, p. 120287, 2021. ISSN 00223093.

48 HUANG, B. *et al.* Effects of Er3+ concentration on upconversion luminescence and temperature sensing properties in Bi4Ge3O12 crystal. **Journal of Alloys and Compounds**, v. 853, p. 156970, 2021. ISSN 09258388.

49 YATSKIV, R. *et al.* Temperature sensing down to 4 k with erbium-doped tellurite glasses. **Journal of Non-Crystalline Solids**, v. 575, p. 121183, 2022. ISSN 00223093.

50 NEXHA, A. *et al.* Luminescence nanothermometry using self-assembled Er3+, Yb3+ doped Y2O3 nanodiscs: Might the upconversion mechanism condition their use as primary thermometers? **Optical Materials**, v. 134, p. 113216, 2022. ISSN 09253467.

51 LAIA, A. S. *et al.* Temperature sensing with Er3+ doped Y2O3 nanoparticles operating within the 1st and 2nd biological window: The influence of particle size on the relative sensitivity of thermally decoupled levels. **Journal of Alloys and Compounds**, v. 926, p. 166816, 2022. ISSN 09258388.

52 KREIDT, E. *et al.* **Nonradiative deactivation of lanthanoid luminescence by multiphonon relaxation in molecular complexes**. Amsterdam: Elsevier, 2018.

53 TAME, M. S. *et al.* Quantum plasmonics. **Nature Physics**, v. 9, p. 329–340, 2013. ISSN 1745-2473.

54 PINES, D. A collective description of electron interactions: Iv. electron interaction in metals. **Physical Review**, v. 92, p. 626–636, 1953. ISSN 0031-899X.

55 HOPFIELD, J. J. Theory of the contribution of excitons to the complex dielectric constant of crystals. **Physical Review**, v. 112, p. 1555–1567, 1958. ISSN 0031-899X.

56 RITCHIE, R. H. Plasma losses by fast electrons in thin films. **Physical Review**, v. 106, p. 874–881, 1957. ISSN 0031-899X.

57 ELSON, J. M.; RITCHIE, R. H. Photon interactions at a rough metal surface. **Physical Review B**, v. 4, p. 4129–4138, 1971. ISSN 0556-2805.

58 ZHANG, J. *et al.* Surface plasmon polaritons: physics and applications. **Journal of Physics D**, v. 45, p. 113001, 2012. ISSN 0022-3727.

59 KUMAR, G.; SARSWAT, P. K. **Interaction of surface plasmon polaritons with nanomaterials**. Berlin: Springer, 2016. 103-129 p.

60 WEINER, J. The physics of light transmission through subwavelength apertures and aperture arrays. **Reports on Progress in Physics**, v. 72, p. 064401, 2009. ISSN 0034-4885.

61 GONCALVES, P. A. D. *et al.* Plasmon–emitter interactions at the nanoscale. **Nature Communications**, v. 11, p. 366, 2020. ISSN 2041-1723.

62 ZHONG, J.-H. *et al.* Nonlinear plasmon-exciton coupling enhances sum-frequency generation from a hybrid metal/semiconductor nanostructure. **Nature Communications**, v. 11, p. 1464, 2020. ISSN 2041-1723.

63 RIVERA, N.; KAMINER, I. Light–matter interactions with photonic quasiparticles. **Nature Reviews Physics**, v. 2, p. 538–561, 2020. ISSN 2522-5820.

64 SILVA, O. B. *et al.* Germanium concentration effects on the visible emission properties of Er3+ in tellurite glasses. **Journal of Luminescence**, North-Holland, v. 232, p. 117808, 2021. ISSN 00222313.

65 FRIEDENSEN, S. *et al.* Materials analysis and focused ion beam nanofabrication of topological insulator bi2se3. **Scientific Reports**, v. 7, p. 13466, 2017. ISSN 2045-2322.

66 ELISA, M. *et al.* Synthesis and characterization of pld glass phosphate films doped with CdS. **Journal of Materials Science**, Springer, v. 52, p. 2895–2901, 2017. ISSN 15734803.

67 CHEN, C. *et al.* Radio frequency magnetron sputtering deposition of TiO2 thin films and their perovskite solar cell applications open. **Scientific Reports**, v. 5, p. 17684, 2015.

68 ASTINCHAP, B.; LAELABADI, K. G. Effects of substrate temperature and precursor amount on optical properties and microstructure of cvd deposited amorphous TiO2 thin films. **Journal of Physics and Chemistry of Solids**, v. 129, p. 217–226, 2019. ISSN 00223697.

69 MAMMERI, F. Nanostructured flexible pvdf and fluoropolymer-based hybrid films. **Frontiers of Nanoscience**, Elsevier, v. 14, p. 67–101, 2019. ISSN 1876-2778.

70 YILBAS, B. S. *et al.* **Surfaces for self-cleaning**. Amsterdam: Elsevier, 2019.

71 CLABEL, J. *et al.* Insights on the mechanism of solid state reaction between tio2 and baco3 to produce batio3 powders: The role of calcination, milling, and mixing solvent. **Ceramics International**, v. 46, p. 2987–3001, 2020. ISSN 02728842.

72 CLABEL, J. L. *et al.* Understanding the electronic properties of BaTiO3 and Er3+ doped BaTiO3 films through confocal scanning microscopy and xps: the role of oxygen vacancies. **Physical Chemistry Chemical Physics**, v. 22, p. 15022–15034, 2020. ISSN 1463-9076.

73 BOUDRIOUA, A. *et al.* Organic light-emitting diodes. **Organic Lasers**, Elsevier, p. 49–93, 2017.

74 ZHANG, J. X.; HOSHINO, K. **Fundamentals of nano/microfabrication and scale effect**. New York: Academic Press, 2019.

75 CLABEL, J. *et al.* Near-infrared light emission of Er3+-doped zirconium oxide thin films: An optical, structural and xps study. **Journal of Alloys and Compounds**, v. 619, p. 800–806, 2015. ISSN 09258388.

76 CLABEL, J. *et al.* Activation energy and its fluctuations at grain boundaries of Er3+:BaTiO3 perovskite thin films: Effect of doping concentration and annealing temperature. **Vacuum**, v. 194, p. 110562, 2021. ISSN 0042207X.

77 GHOSH, G. Sellmeier coefficients and dispersion of thermo-optic coefficients for some optical glasses. **Applied Optics**, v. 36, p. 1540, 1997. ISSN 0003-6935.

78 FISCHER, H. E. *et al.* Neutron and x-ray diffraction studies of liquids and glasses. **Reports on Progress in Physics**, IOP Publishing, v. 69, p. 233, 2005. ISSN 0034-4885.

79 JAIN, A. *et al.* The materials project: A materials genome approach to accelerating materials innovation. **APL Materials**, American Institute of Physics Inc., v. 1, 2013. ISSN 2166532X.

80 RICALDI, J. C. *et al.* Influence of Pr3+ ions on the structural properties of Er3+-doped tellurite-tungsten glasses. **Journal of Non-Crystalline Solids**, v. 616, 2023. ISSN 18734812.

81 SHEN, S. *et al.* Tungsten–tellurite—a host glass for broadband edfa. **Optics Communications**, North-Holland, v. 205, p. 101–105, 2002. ISSN 0030-4018.

82 HOU, G. *et al.* 2.0-µm and 4.1-µm mid-infrared broadband emission enhancement in Ho3+/Yb3+ co-doped tellurite–germanate glasses. **Journal of Materials Science**, v. 31, p. 2057–2062, 2020. ISSN 0957-4522.

83 MOTT, N.; DAVIS, E. **Electronic processes in non-crystalline materials**. London: Oxford University Press, 2012.

84 TAUC, J.; MENTH, A. States in the gap. **Journal of Non-Crystalline Solids**, North-Holland, v. 8-10, p. 569–585, 1972. ISSN 0022-3093.

85 RIVERA, V. A. G. *et al.* Plasmon-photon conversion to near-infrared emission from Yb3+: (Au/Ag-nanoparticles) in tungsten-tellurite glasses. **Scientific Reports**, v. 6, p. 18464, 2016. ISSN 2045-2322.

86 JLASSI, I. *et al.* Thermal and optical properties of tellurite glasses doped erbium. **Journal of Materials Science**, Kluwer Academic Publishers, v. 46, p. 806–812, 2011. ISSN 15734803.

87 GONCALVES, A. *et al.* Luminescence and upconversion processes in Er3+ -doped tellurite glasses. **Journal of Luminescence**, v. 201, p. 110–114, 2018. ISSN 00222313.

88 SESHADRI, M. *et al.* Optical characterization, infrared emission and visible up-conversion in Er3+ doped tellurite glasses. **Journal of Non-Crystalline Solids**, v. 402, p. 141–148, 2014. ISSN 00223093.

89 JHA, A. *et al.* Structural origin of spectral broadening of 1.5-μm emission in Er3+-doped tellurite glasses. **Physical Review B**, v. 62, p. 6215–6227, 2000. ISSN 0163-1829.

90 SHEN, S. *et al.* Compositional effects and spectroscopy of rare earths (Er3+, Tm3+, and Nd3+) in tellurite glasses. **Comptes Rendus Chimie**, Elsevier, v. 5, p. 921–938, 2002. ISSN 1631-0748.

91 URBACH, F. The long-wavelength edge of photographic sensitivity and of the electronic absorption of solids. **Physical Review**, v. 92, p. 1324–1324, 1953. ISSN 0031-899X.

APPENDIX

APPENDIX A – CALCULATION OF THE OPTICAL BANDGAP USING THE METH-TAUC AND URBACH MODELS

While investigating amorphous germanium's optical and electronic properties, Tauc*et al.*, 1972 [84] proposed a method for determining the band gap using optical absorbance data. Davis and Mott, 2012[83] later expanded this approach, in their comprehensive study of amorphous semiconductors. They demonstrated that the optical absorption strength is dependent on the difference between photon energy and the band gap and can be described by the equation: micro spectrometer

$$(\alpha h v)^{1/n} = A\left(hv - E_{\mathrm{g}}\right) \tag{A.1}$$

where h is Planck's constant, v is the photon's frequency, α is the absorption coefficient, E_{g} is the band gap, and A is a proportionality constant. The value of the exponent denotes the nature of the electronic transition. Typically, allowed transitions dominate the basic absorption processes, giving either $n = 1/2$ or $n = 2$, for direct and indirect transitions, respectively. On the other hand, in the case of non-crystalline semiconductors, the absorption coefficient exhibits an exponential dependence on the energy of incident photons near the edge of the optical bandgap. This region is characterized by lower photon energy compared to the bandgap and can be described by the equation:

$$\alpha = B \exp(h\nu/E_U) \tag{A.2}$$

where B is a proportionality constant and E_U represents the Urbach Energy, indicating the level of structural disorder in the non-crystalline material. The value of E_U is determined by calculating the inverse of the slope of the tangent line to the linear portion of the $ln\alpha$ curve.[91]

Figure 40.a and 40.b shows the graphs with which the bandgap energies were determined by plotting the $(\alpha hv)^{1/n}$ vs. (hv).

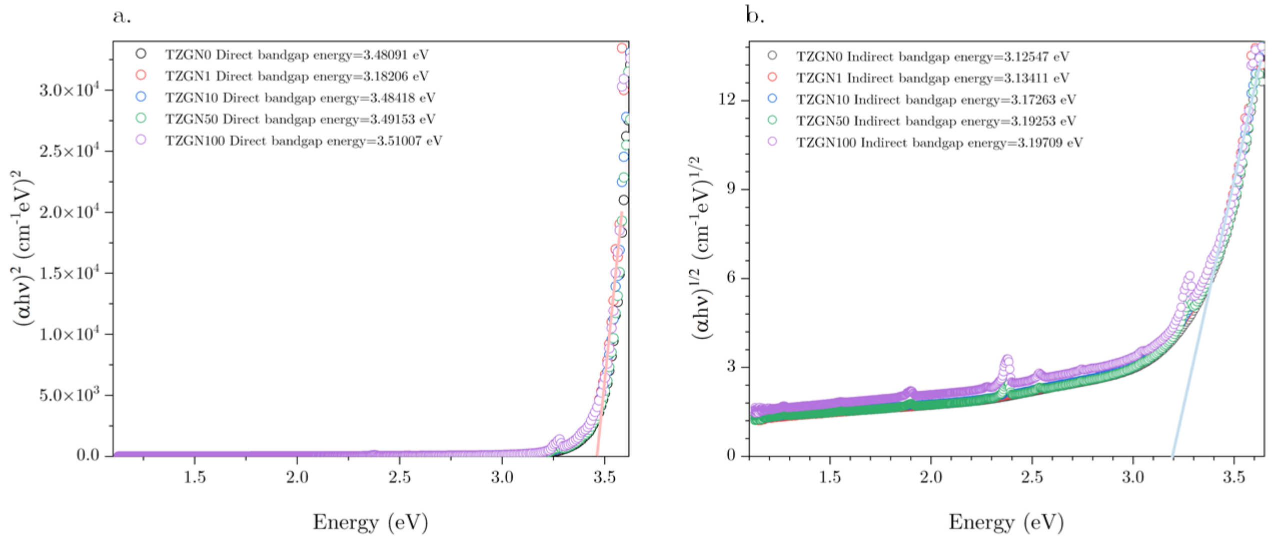

Figure 40 – Direct and indirect bandgaps of TZGN glasses.

Source: By the author

Figure 41 shows the Urbach energies, calculated by the inverse of the slope of the tangent line to the linear part of the curve $ln\alpha$.

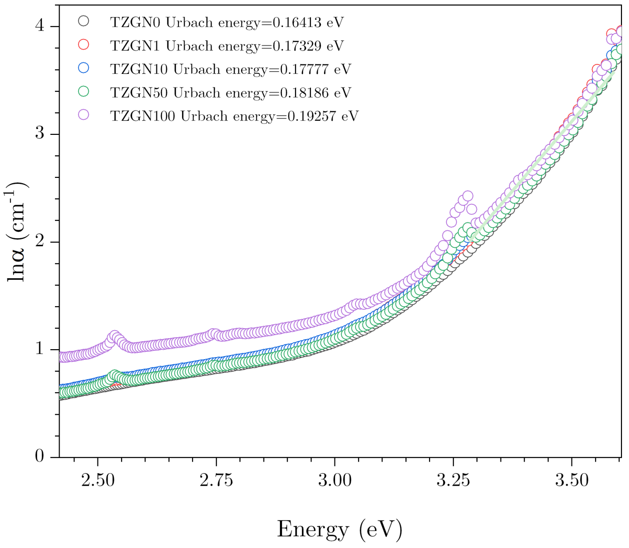

Figure 41 – Urbach energies of TZGN glasses.

Source: By the author

APPENDIX B – DECOMPOSITION OF THE RAMAN SPECTRA

Decomposition of the Raman spectra was performed with the OriginPro software and is presented in Figure 42. A value of R^2=0.999% was obtained, and the Raman bands identified in the decomposition are reported in Table 7.

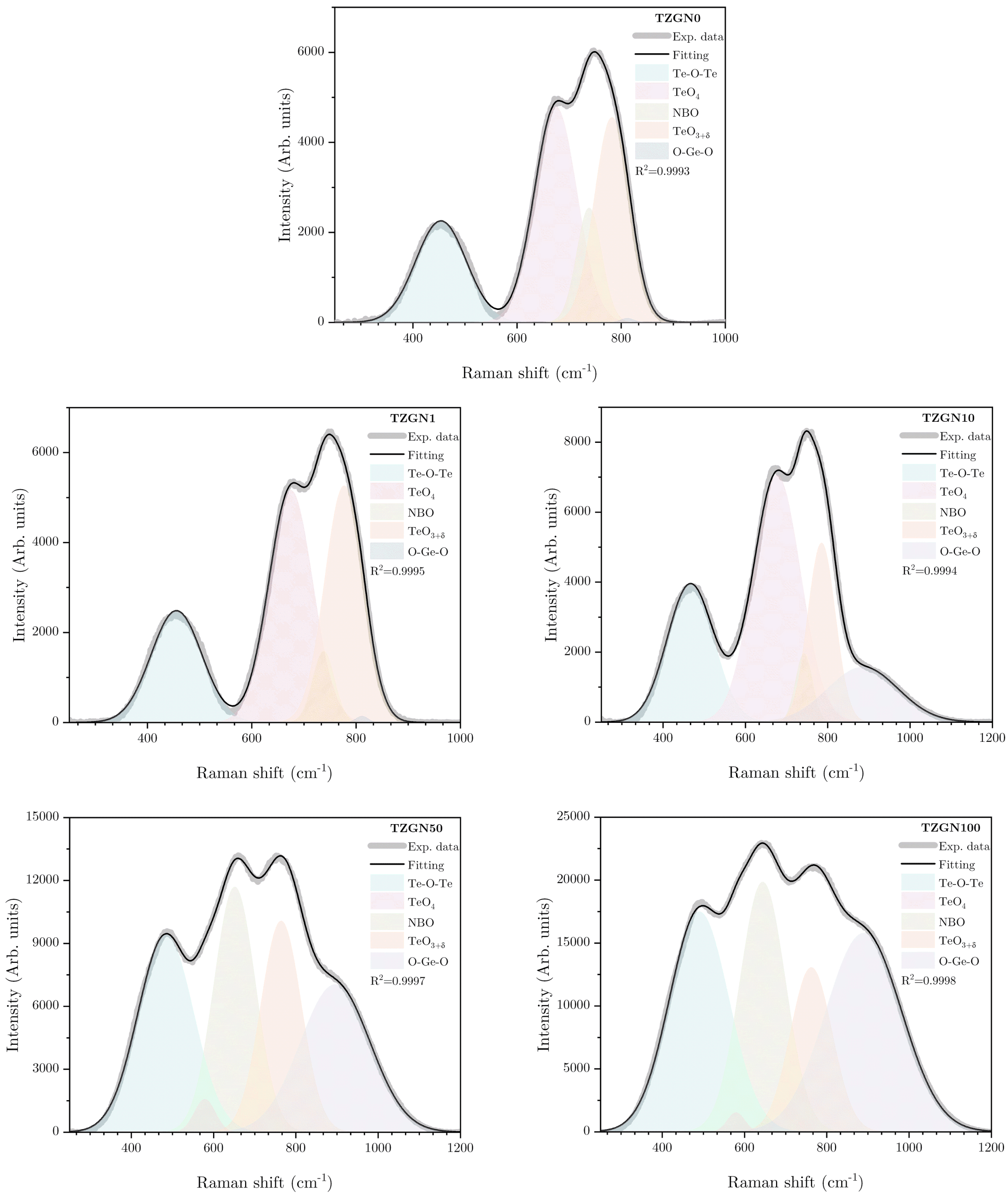

Figure 42 – Deconvoluted Raman spectra of TZGN glasses.

Source: By the author

Table 7 – Assigned Raman bands of TZGN glasses.

Asigened vibrational modes in TZGN glasses	Raman bands in the literature (cm^{-1})
Stretching and bending vibration of O–Te–O linkages in TeO_4, TeO_{3+1} and TeO_3	$\sim$450
Vibration of the continuous network comprised of TeO_4	$\sim$660
Stretching vibrations between tellurium and non-bridging oxygen (NBO) atoms	$\sim$715
Continuous network vibration of TeO_4 and a TeO^- stretching vibration of TeO_{3+1} or TeO_3	$\sim$775
Asymmetric stretching vibrations of O–Ge–O in tetrahedral GeO_4	$\sim$820

Source: Adapted from JHA *et al.*, 2012.[27]

APPENDIX C – FLUORESCENCE LIFETIME IMAGE OF Er^{3+}-DOPED GLASS

Figure 43 shows the images and hyperspectra of TZGN5 glass with an Au film deposit on its surface under 1 mW/980 nm excitation.

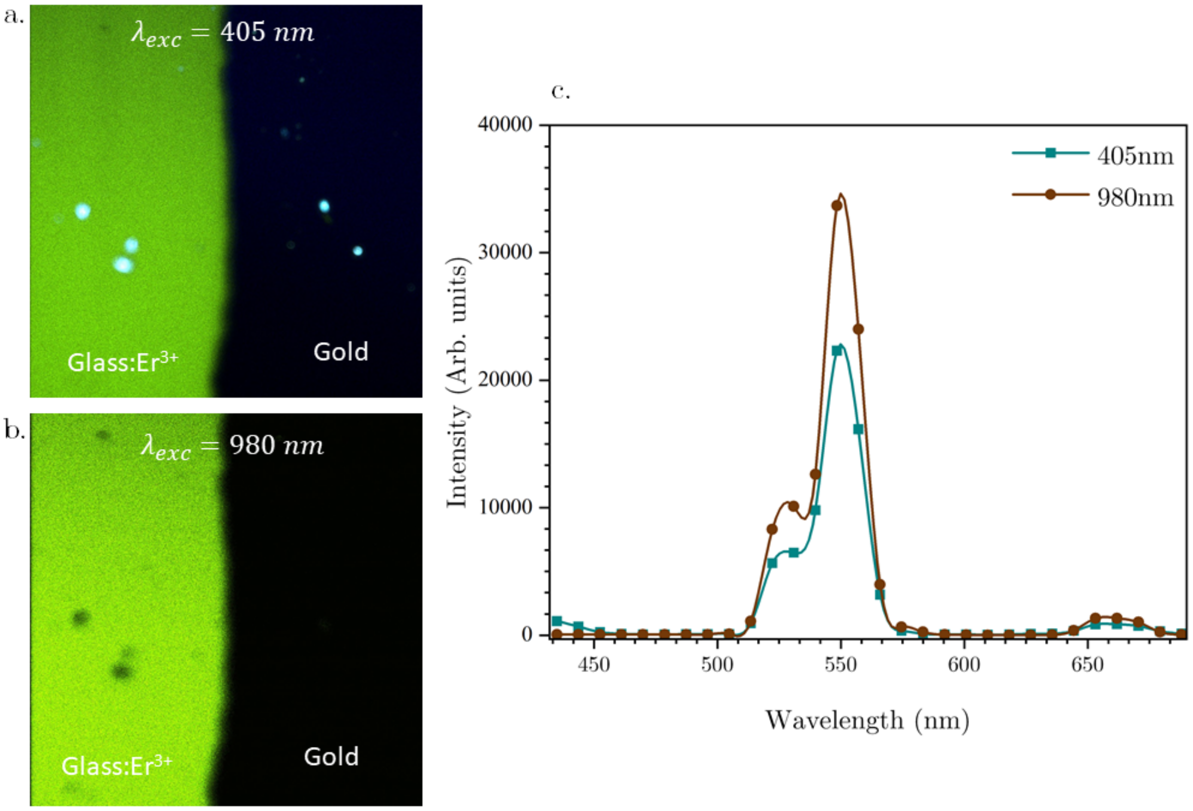

Figure 43 – Confocal microscopy measurement of TZGN5 glass.

Source: By the author

The fluorescence lifetime images were measured with the same conditions and in the same region as the spectral image in Channel 1 (CH1, green region) and Channel 2 (CH2, red region), with $\lambda_{exc} = 405$ nm (see Figure 44) and $\lambda_{exc} = 980$ nm (see Figure 45) it was observed that the lifetime scale is of the order of ns, but the scale of the lifetime of the Er^{3+} ions in this regions is of the order of μs, for which reason only the background of the decay curve is observed.

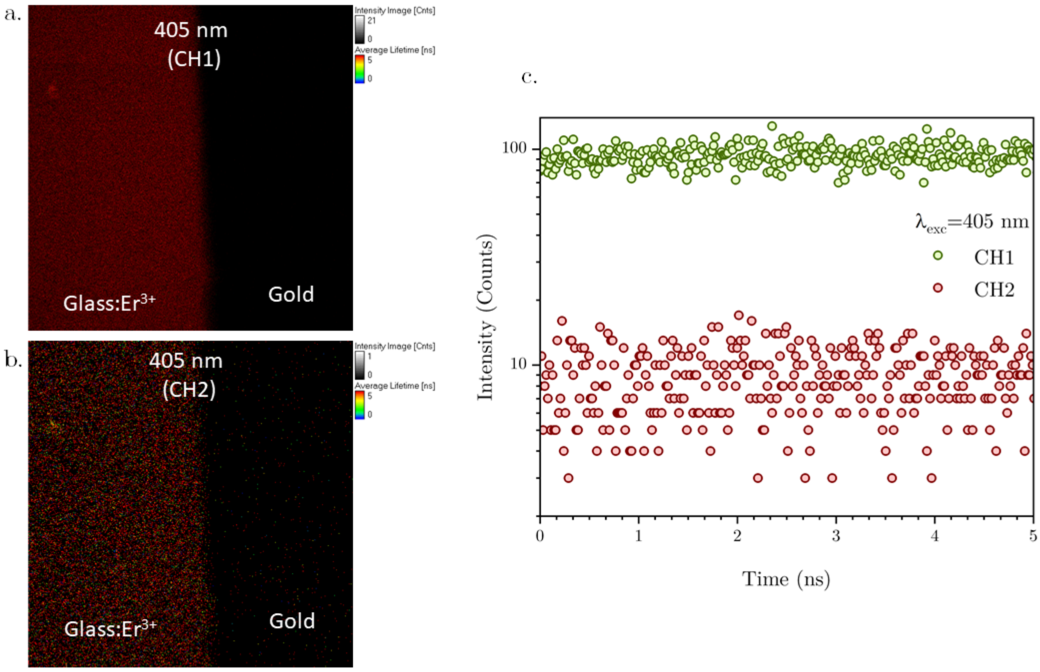

Figure 44 – Fluorescence lifetime image of TZGN5 glass under 405 nm, a. CH1, b. CH2 and c. Lifetime decay curve

Source: By the author

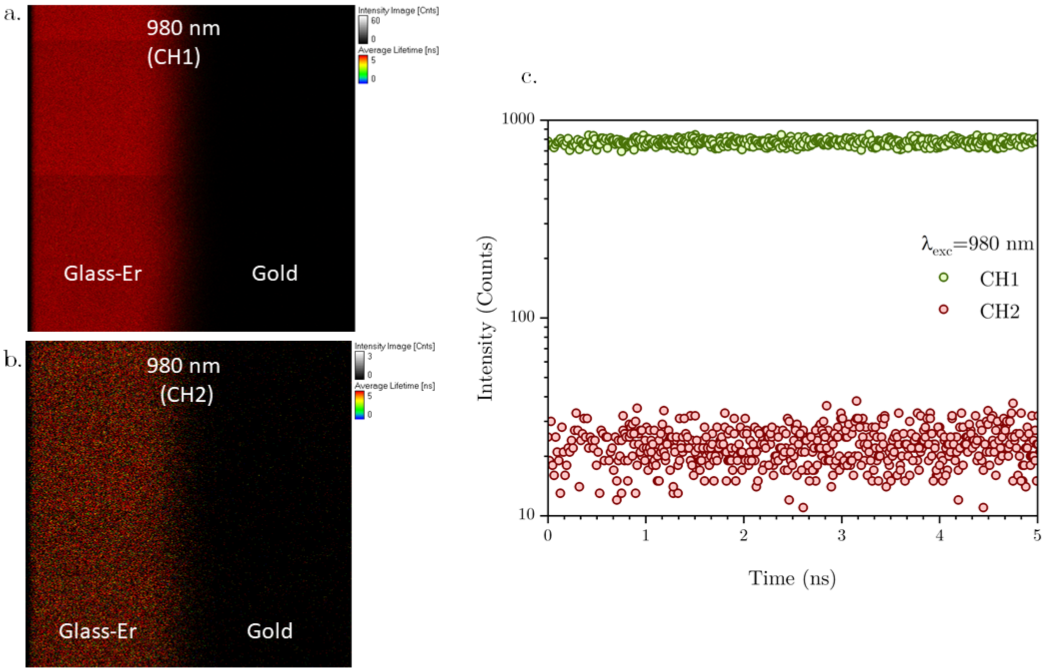

Figure 45 – Fluorescence lifetime image of TZGN5 glass under 980 nm, a. CH1, b. CH2 and c. Lifetime decay curve

Source: By the author

APPENDIX D – APROXIMATION OF Er^{3+} QUANTY FOR SINGLE NANOGLASS

In this chapter, we present calculations to approximate the amount of Er^{3+} ions found in a single nanoglass. Consider a spherical nanoglass with an approximate diameter of 300 nm, the radius of the nanoglass would be 150 nm. The volume of the nanoglass is calculated with the formula:

$$V_{ng} = \frac{4}{3}\pi r^3 = 4188790.205\ nm^3 \tag{D.1}$$

In Table 8, the Er^{3+} concentrations per nm^3 were presented.

Table 8 – Er^{3+} concentrations per nm^3 (C$_{Er}$).

Sample	Concentration (ions/nm^3)
TZGN0	0
TZGN1	4.739×10^{-4}
TZGN10	4.797×10^{-3}
TZGN50	2.604×10^{-2}
TZGN100	5.219×10^{-2}

So, to calculate the quanty of Er^{3+}/nanoglass ions, the formula is used:

$$C_{Er} \times V_{np} = I_{np} \tag{D.2}$$

In Table 9, the Er^{3+} concentrations per nanoglass were presented.

Table 9 – Er^{3+} concentrations per nanoglass.

Sample	Concentration (ions/nanoglass)
TZGN0	0
TZGN1	∼1985
TZGN10	∼20093
TZGN50	∼109076
TZGN100	∼218612

These calculations are merely approximate since the nanoglass's shape is irregular and not spherical.

ANNEX

ANNEX A – INSTRUMENTATION AND SCHEMATIC REPRESENTATION OF LASER SCANNING CONFOCAL FLUORESCENCE MICROSCOPY

The schematic representation of Invert Zeiss LSM 780 multiphoton laser scanning confocal fluorescence microscope is shown in Figure 46 shows a schematic representation of the LSCF instrumentation. It can be divided into three parts: 1) laser combination and selection module, 2) confocal scanning imaging and multichannel spectral imaging module, and 3) microscope.

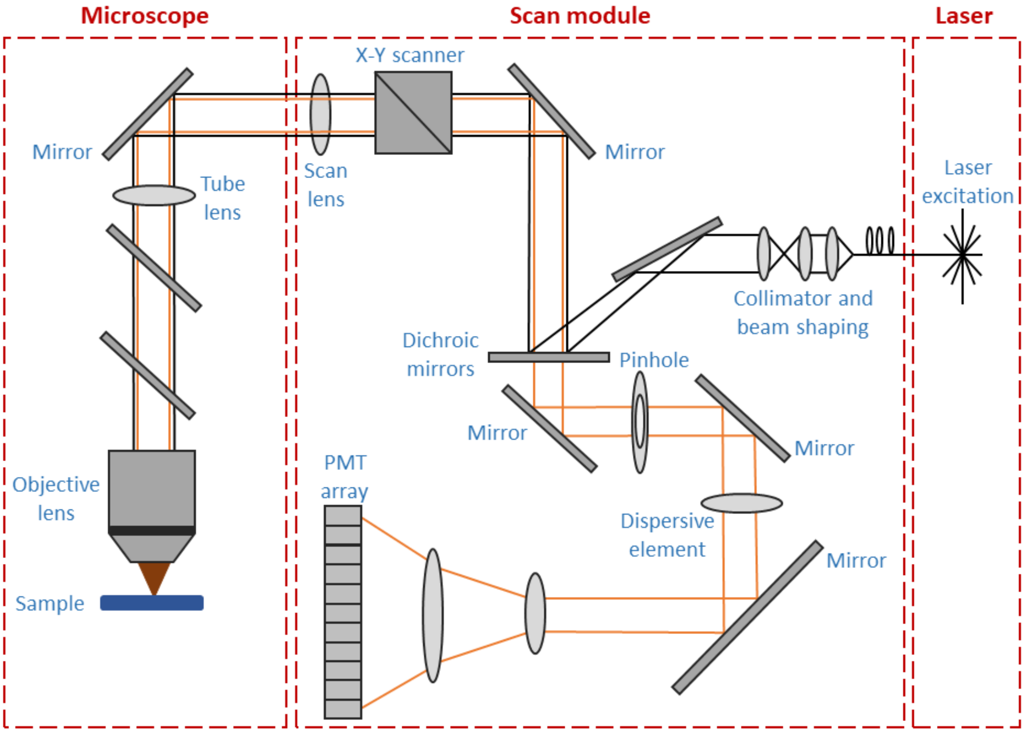

Figure 46 – Instrumentation and schematic representation of laser scanning confocal fluorescence microscopy.

Source: Adapted from CLABEL *et al.*, 2020.[72]

ANNEX B – MAXWELL EQUATIONS OF PLASMON DYNAMICS

The dynamics of plasmons are based on the interaction of electromagnetic waves with matter, which is governed by Maxwell's equations. To begin with, boundary conditions are applied at the metal-dielectric interface for the electric fields **E** and magnetic fields **H**. Quantum emitters are considered as oscillating dipoles, whose radiation can be decomposed into an integral over plane waves. So, according to Fresnel's theory for the refraction of plane waves in planar dielectric structures, the integrals for the electromagnetic fields for an arbitrary point in the structure are:

$$\begin{aligned}\mathbf{E} = i\frac{\mu_0 c^2 k_0^3}{4\pi n n_\mathrm{d}}\mathbf{p}\int_0^\infty dn_\rho \frac{n_\rho^2}{\sqrt{n_\mathrm{d}^2 - n_\rho^2}}&\Big[i\widehat{\boldsymbol{\rho}}_r n_\mathrm{z}\mathrm{J}_1\left(k_0 n_\rho \rho\right)\left(a\mathrm{e}^{ik_0 n_\mathrm{z}\mathrm{z}} - be^{-ik_0 n_\mathrm{z}\mathrm{z}}\right) \\ &-\hat{\mathbf{z}} n_\rho \mathrm{J}_0\left(k_0 n_\rho \rho\right)\left(a\mathrm{e}^{ik_0 n_\mathrm{z}\mathrm{z}} + \mathrm{b}e^{-ik_0 n_\mathrm{z}\mathrm{z}}\right)\Big]\end{aligned} \tag{B.1}$$

$$\mathbf{H} = -\frac{k_0^3 c^2}{4\pi}\mathbf{p}\int_0^\infty dn_\rho \frac{n_\rho^2}{\sqrt{n_\mathrm{d}^2 - n_\rho^2}}\left[\widehat{\boldsymbol{\varphi}}_\mathbf{r}\mathrm{J}_1\left(k_0 n_\rho \rho\right)\left(ae^{ik_0 n_\mathrm{z}\mathrm{z}} + be^{-ik_0 n_\mathrm{z}\mathrm{z}}\right)\right] \tag{B.2}$$

where n_d is the refractive index of the medium containing the quantum emitter, $n_\rho = k_\rho/k_0$ where k_ρ is the component of the wave vector parallel to the plane of the structure, $n_z = k_z/k_0$ where k_z is the z component of the wave vector, c is the speed of light in a vacuum, μ_0 is the magnetic permeability of the vacuum, a and b are coefficients associated with the waves, J_m are the Bessel functions of order m, $\widehat{\boldsymbol{\varphi}}_\mathbf{r}$ is the unit vector of azimuth direction, $\rho = \sqrt{x^2 + y^2}$ and $\mathbf{p}$ is the dipolar moment of the quantum emitter.